HORIZON EUROPE PROGRAMME
HORIZON-JTI-CLEANH2-2024

GA No. 101192342

Direct seawater electrolysis technology for distributed hydrogen production

SWEETHY

SWEETHY - Deliverable report

D3.1. – Catalysts preparation and characterisation for direct operation with seawater

Clean Hydrogen Partnership

Co-funded by the European Union

Deliverable No.	D3.1.	
Related WP	WP3	
Deliverable Title	Catalysts preparation and characterisation for direct operation with seawater	
Deliverable Date	2025-12-31	
Deliverable Type	Report	
Dissemination level	Public (PU)	
Author(s)	Carmen Tébar Soler (CIDETEC), Aliona Nicolenco (CIDETEC), Francisco Alcaide (CIDETEC) Sabrina C. Zignani (CNR), Mariarosaria Pascale (CNR), Marta Fazio (CNR), Nicola Briguglio (CNR), Bryan Mondello (CNR), Antonino S. Aricò (CNR) Yejung Choi (SINTEF)	2025-12-16
Checked by	Francisco Alcaide (CID)	2025-12-23
Reviewed by	Olesia Danyliv (RISE)	2025-12-23
Approved by	Olesia Danyliv (RISE)	2025-12-23
Status	Final	2025-12-23

Project Summary

SWEETHY will develop an advanced technology for direct seawater electrolysis that will be able to produce H_2 and O_2 under intermittent conditions accounting for the coupling to renewable power sources (especially wind, PV). The electrolyser will be based on an anion exchange membrane (AEM) operating in natural or alkaline seawater, and the SWEETHY technology will be developed along three dimensions:

a) Materials optimisation. To meet the specific requirement of seawater environment the project will focus on corrosion resistance and selective PGM-free electrocatalysts for hydrogen and oxygen evolution reactions, on AEM with high selectivity for transporting hydroxide anions and anti-fouling properties as well as on novel anti-corrosion coatings for bipolar plates and porous transport layers prepared by plasma spraying and electrodeposition.

b) Electrolyser stack prototyping. The project will exploit a novel stack architecture, which uses hydraulic cell compression to host the advanced materials and to produce H_2 at high pressure. Beneficial functions of the targeted unique stack are related to scalability and maintainability that will be tremendously improved in comparison to conventional AEMWE stacks.

c) Sustainability analysis. The project will conduct studies (life-cycle assessment (LCA), techno-economic analysis (TEA)) to evaluate circularity of the electrolyser system and its integration into renewable-power systems and to explore an efficient by-product utilisation way through industrial symbioses. These studies will feed back to materials optimisation and stack development. Complementing LCA, social LCA and techno-economic analyses/optimisation by qualitative work ensures both environmental, economic, and social sustainability.

Combining these three dimensions, SWEETHY will utilise Mediterranean seawater from the coast of Messina, Italy, to test its electrolyser with the goal withstand more than 2000 h of operation to produce 20 g_{H2}/h with a degradation rate lower than 1%/100h. In addition, SWEETHY will demonstrate how the operation of the electrolyser can ensure an optimised revenue concerning by-products and grid services.

Public Deliverable Summary

Deliverable 3.1 reports the progress of Work Package 3 (WP3) toward developing PGM-free electrocatalysts for the hydrogen evolution reaction (HER) and oxygen evolution reaction (OER) under direct seawater electrolysis conditions. The work focuses on designing, synthesizing, and optimizing non-noble, earth-abundant catalyst materials capable of resisting chloride-induced corrosion while ensuring high activity, durability, and scalability for alkaline anion-exchange membrane water electrolysis (AEMWE).

The deliverable covers two main tasks:

Task 3.1 – HER catalysts, covering transition-metal chalcogenides, carbides, phosphides, and Ni-based alloys (powders and self-standing electrodes);

Task 3.2 – OER catalysts, focusing on nanosized mixed metal oxides, layered double hydroxides (LDHs) and alloys.

The materials were synthesized by three SWEETHY partners (CIDETEC, CNR, SINTEF) using wet-chemistry, hydrothermal, solid-state, electroless deposition, and electrodeposition approaches, followed by extensive physicochemical characterization (XRD, SEM/TEM, EDX/XRF).

For HER, nickel- and molybdenum-based systems including NiS_2, MoS_2, Mo_2C, Ni-Mo alloys, and ternary Ni-Mo-S films were synthesized and structurally optimized. Strategies such as carbon supports, nanostructuring and controlled alloying enabled tunable crystallinity, surface area and composition. Self-standing electrodes (Ni-felt or nano-PTLs coated with Ni-Mo or Ni_3S_2) were successfully fabricated, demonstrating tunable Mo/S content, and scalable fabrication. Benchmark Pt/C was fully characterized for comparison.

For OER, several families of PGM-free catalysts were produced, including NiFe-LDH and NiMn-LDH, NiFe spinels, showing nanometric crystallite sizes and suitable layered or spinel structures. Complementary approaches yielded self-standing Ni-W, Ni-Co, and Ni-P foams, enabling porous architectures and controlled composition. Benchmark Co_3O_4 was also analysed for reference.

Most catalysts were successfully scaled from gram-scale (2 g) to medium-scale (6 g) batches without loss of structural or compositional quality, confirming the suitability of the selected synthesis routes for future industrial upscaling.

Overall, Deliverable 3.1 establishes a validated portfolio of PGM-free HER and OER catalysts compatible with the harsh conditions of seawater electrolysis. These materials directly support SWEETHY's Specific Objective 1, providing low-cost, durable catalyst candidates and benchmark references for subsequent electrochemical testing, integration into large-area electrodes (WP6), cost and sustainability analyses (SO3–SO4), and ultimately the construction of the SWEETHY seawater-AEMWE prototype. The deliverable also generates exploitable scientific and technological know-how on catalyst design, alloying, nanostructuring, and scalable synthesis for seawater-resistant electrolysis.

Contents

List of Figures

List of Tables

1 Introduction

Deliverable 3.1 ***"Catalysts preparation and characterisation for direct operation with seawater"*** reports the progress and results achieved by M10 within Work Package 3 (WP3), which focuses on the development of PGM-free electrocatalysts for hydrogen (HER) and oxygen evolution reactions (OER) under seawater-electrolysis relevant conditions. The activities presented in this deliverable cover the preparation and physicochemical optimization (structural, compositional, morphological characterization) of catalyst materials designed for direct operation in sea water environment. The deliverable reports on the results obtained under (i) ***Task 3.1 - Hydrogen evolution electrocatalysts (HER)*** covering the development of PGM-free cathode materials based on transition metal chalcogenides, phosphides, carbides, and Ni-based alloys, as well as fabrication of self-standing electrodes via electrodeposition and nanostructuring approaches; and (ii) ***Task 3.2 - Oxygen evolution electrocatalysts (OER)*** dealing with the development of PGM-free anode materials derived from nanosized mixed metal oxides and layered double hydroxides (LDHs) optimised for stability and activity in seawater electrolysis conditions. This report summarises the methodologies used for catalyst synthesis developed by the WP3 partners (CIDETEC, CNR, SINTEF) including wet-chemistry and electrochemical routes, thermal and structural stabilisation procedures and the physicochemical characterisation of the obtained materials.

2 Hydrogen evolution electrocatalysts

2.1 PGM-free metal powder cathode electrocatalysts

PMG-free metal powder cathode electrocatalysts are catalytic materials that exclude platinum group metals (PGMs) such as Pt, Pd, and Rh, with the objective of reducing cost and dependence on critical raw materials. These catalysts are typically based on earth-abundant transition metals (e.g., Fe, Ni, Mo) and their compounds. In this context, the PGM-free cathode catalysts developed within the SWEETHY project have been developed using transition metals such as Ni and Mo, as well as their alloys and chalcogenides. Emphasis has been placed on structural optimization and heteroatom doping to improve catalytic activity, electrical conductivity, and durability. The catalysts have been synthesized as nanosized particles supported on carbon-based substrates to maximize surface area and accessibility of active sites.

2.1.1 Nickel sulfide (NiS_2)

Synthesis protocol (CIDETEC)

The NiS_2 catalyst was synthesized by a hydrothermal method. Specifically, nickel and sulphur precursors were each dissolved in ultrapure water and loaded into a Teflon-coated stainless-steel autoclave. The autoclave was placed in an oven, kept under static conditions at the desired temperature for a specified period. Afterwards, the autoclave was removed from the oven and cooled to room temperature. The contents of the autoclave were then filtered under vacuum, recovering a

black solid. The solid was washed using an ultrasonic bath, first twice with ethanol and then three times with ultrapure water. Finally, the material was dried in an oven overnight.

The same hydrothermal protocol was applied for the synthesis of NiS_2/C, with the addition of a carbon source to the precursor solution containing Ni and S.

Physicochemical characterization of obtained catalyst

The crystalline structure of the catalysts was confirmed by X-ray diffraction (XRD), as shown in Figure 1. Measurements were performed using a Bruker D8 diffractometer with Cu Kα radiation (λ = 0.15406 nm) in the Bragg–Brentano geometry. Both samples display a well-defined diffraction pattern characteristic of cubic NiS_2. The main diffraction peaks appear at 2θ values of 27.2°, 31.5°, 35.3°, 38.8°, 45.2°, 53.5°, 56.1°, 58.6°, 61.1°, 68.2°, 72.5°, 74.7°, and 76.9°, corresponding to the (111), (200), (201), (211), (220), (311), (222), (023), (321), (410), (331), (024), and (421) planes, respectively (PDF#01-078-4702).

In addition to the main NiS_2 reflections, small peaks were observed at 18.8°, 20.1°, and 22.2°, which are more pronounced in the NiS_2/C sample. These additional reflections are attributed to residual precursors, arising from incomplete reaction during synthesis, and are not associated with the crystalline NiS_2 phase.

The crystallite size of the NiS_2 sample was estimated to be 15 nm using the Scherrer equation, with lattice parameters a = b = c = 5.67 Å, in agreement with theoretical values. For the NiS_2/C composite, both the crystallite size and the lattice parameter remained constant. These results confirm that the incorporation of the carbon source does not significantly affect the crystal structure of NiS_2.

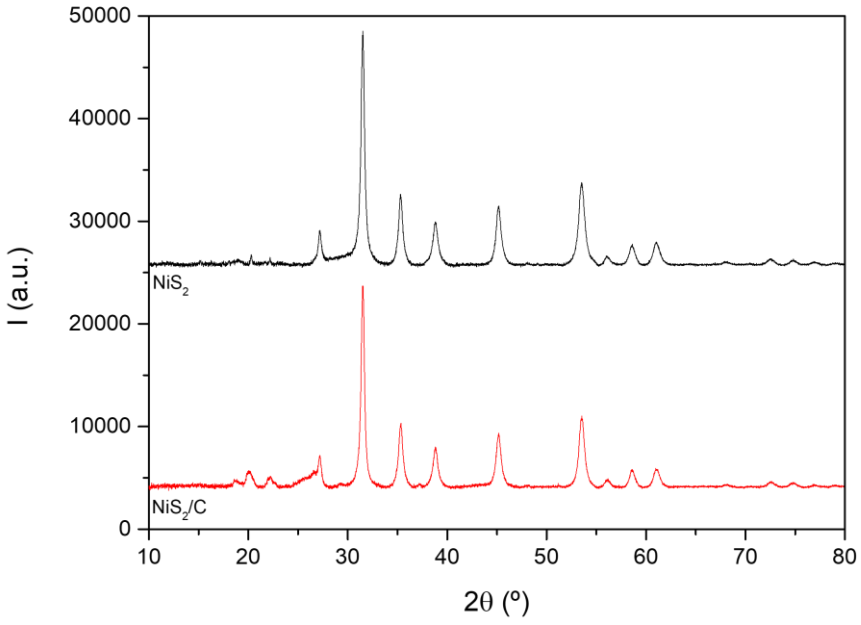

Figure 1. X-ray diffraction patterns of NiS_2 (in black) and NiS_2/C (in red).

The sample morphology was examined by Scanning Electron Microscopy (SEM) (Carl Zeiss Ultra Plus). Figure 2 shows the SEM images of NiS_2 (a) and NiS_2/C (b). Figure 2a displays a relatively uniform distribution of spherical like NiS_2 nanoparticles. In Figure 2b, the NiS_2 particles are also spherical like and appear to be well-dispersed on the carbon support.

The composition of the catalysts was determined using an Energy Dispersive X-ray (EDX) with an OXFORD Xplore 15 detector coupled to the scanning electron microscope, and by X-ray Fluorescence (XRF) with an XDV-SDD analyser from Fisher Instruments, equipped with a silicon drift detector. The results from both techniques are summarized in Table 1.

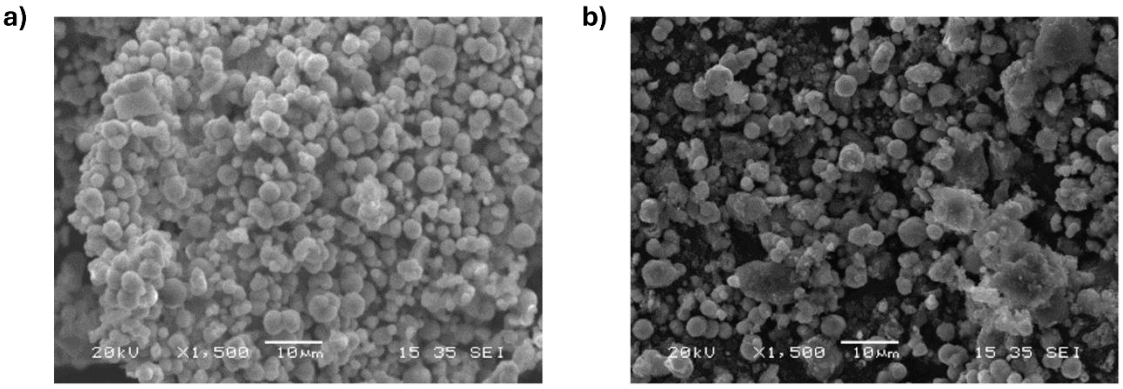

Figure 2. SEM images of NiS_2 (a) and NiS_2/C (b).

Table 1. Elemental composition (% wt.) of NiS_2 and NiS_2/C determined by EDX and XRF analyses

Sample	EDX (% wt.)			XRF (% wt.)		
	Ni	S	C	Ni	S	C
NiS_2	47.33	52.68	-	55.8	44.12	n.d.*
NiS_2/C	18.7	16.4	64.9	59.3	40.8	n.d.*

*n.d.: not detected, indicating that the element is below the detection limit of the technique.

For the NiS_2 sample, both EDX and XRF results are in good agreement, indicating a Ni:S ratio close (Ni:S 1:2) to the expected stoichiometry, which confirms the successful formation of the NiS_2 phase. In the case of NiS_2/C, only the EDX values are considered due to the limitations of XRF in detecting carbon. Based on the EDX analysis, the supported catalyst contains approximately 23 % wt. NiS_2 relative to the total active material, and the Ni:S ratio is also close to the theoretical value. These results confirm the successful incorporation of the active phase onto the carbon support without significant compositional deviations.

Figure 3a shows a Transmission Electron Microscopy (TEM) image of the NiS_2/C sample, revealing the coexistence of particle aggregates and well-defined, predominantly square-shaped like nanoparticles. The particle sizes range approximately from tens to several hundreds of nanometers. The morphological characteristics suggest partial agglomeration and a heterogeneous size distribution within the sample. Figure 3b depicts the particle size distribution histogram derived from a quantitative analysis of particle dimensions measured across multiple TEM micrographs to ensure statistical representativeness. The mean particle size is determined as 140 ± 40 nm.

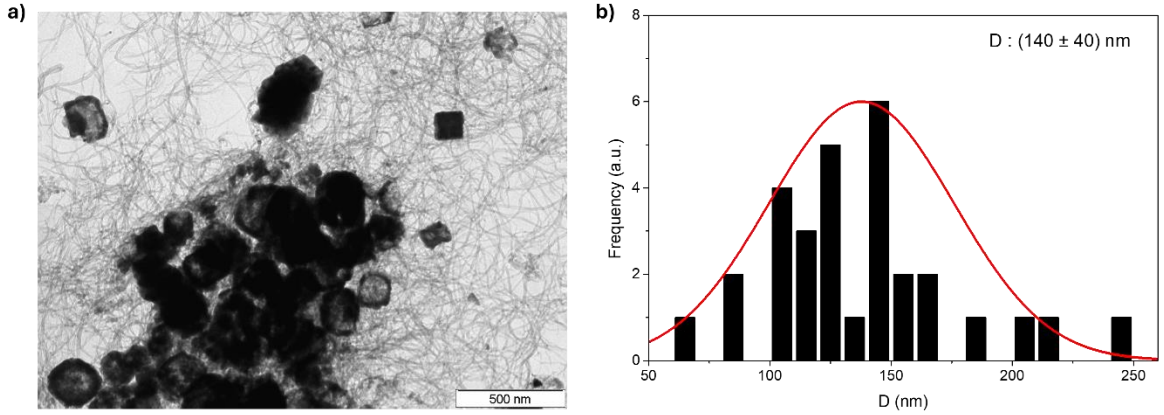

Figure 3. TEM image of NiS_2/C (a) and particle size distribution (b).

Once the synthesis protocol was optimized, the next step was the scale-up of the catalyst from 0.5 g to 1 g. The same experimental procedure, as described previously, was followed, but with proportionally increased reagent quantities. The obtained material is shown in Figure 4. The NiS_2 cubic phase is clearly formed, exhibiting similar crystallite size (14.2 nm) and lattice parameter (5.67 Å) to those obtained in the initial synthesis. The morphology and the composition were confirmed by SEM-EDX and XRF (Figure 4, Table 2). Neither the particle morphology nor the Ni:S atomic ratio (1:2) changed, confirming that the scale-up procedure was successfully achieved. The scale-up of the NiS_2/C material is currently in progress.

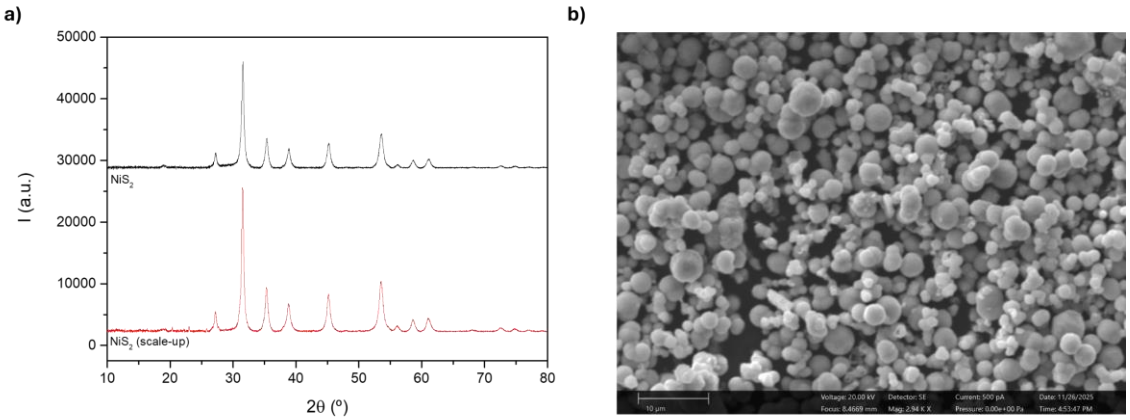

Figure 4. X-ray diffraction patterns of NiS_2 (in black) and NiS_2 scale-up (in red) (a) and SEM image of NiS_2 scale-up (b).

Table 2. Elemental composition (% wt.) of NiS_2 scale-up determined by EDX and XRF analyses.

EDX (% wt.)		XRF (% wt.)	
Ni	S	Ni	S
50.1	49.9	62.5	37.5

2.1.2 Molybdenum disulfide (MoS_2)

Synthesis protocol (CIDETEC)

The MoS_2 catalyst was synthesized by a hydrothermal method. Specifically, a molybdenum precursor and two different sulphur sources (source A for MoS_2-A and source B for MoS_2-B) were each dissolved in ultrapure water and loaded into a Teflon-coated stainless-steel autoclave. The autoclave was placed in an oven and maintained under static conditions at the target temperature for a predetermined duration. Afterwards, the autoclave was removed from the oven and cooled to room temperature. The contents of the autoclave were then filtered under vacuum, recovering a black solid. This solid was subjected to ultrasonic washing: twice with ethanol, followed by three rinses with ultrapure water. Finally, the material was dried overnight in an oven.

The same hydrothermal protocol was applied for the synthesis of MoS_2-A/C composites, with the addition of a carbon source to the Mo and S (source A) precursor solution.

Physicochemical characterization of obtained catalyst

The crystalline structure of the catalysts was confirmed by XRD as shown in Figure 5. All the samples display a diffraction pattern characteristic of hexagonal MoS_2. The main diffraction peaks appear at 2θ values of 13.6°, 28.8°, 32.3°, and 57.5°, corresponding to the (002), (004), (101), and (110) planes, respectively (PDF#00-006-0097). The average crystallite sizes for MoS_2-A (in black) and MoS_2-B (in red) were estimated by the Scherrer equation to be 6.1 nm and 5.0 nm, respectively. The lattice parameters were a = b = 3.1 Å and c = 12.8 Å for MoS_2-A, and a = b = 3.1 Å and c = 12.7 Å for MoS_2-B, consistent with literature values.

The synthesis yields were 20% for MoS_2-A and 10% for MoS_2-B. Despite the relatively low overall yield, source A was chosen for further synthesis on carbon supports and more detailed characterization due to its higher efficiency. Ongoing efforts are aimed at improving the synthesis, for example, by optimizing reaction temperatures, durations, and other parameters.

Regarding the XRD pattern of the MoS_2-A/C (Figure 5, in blue), the main diffraction peaks are consistent with those of MoS_2. For the MoS_2-A/C sample, both the crystallite size (6.4 nm) and lattice parameters (a = b = 3.1 Å, c = 12.8 Å) remain essentially unchanged relative to MoS_2 black. These results indicate

that the incorporation of the carbon source does not significantly alter the crystal structure of MoS_2, though a slight decrease in crystallinity is observed.

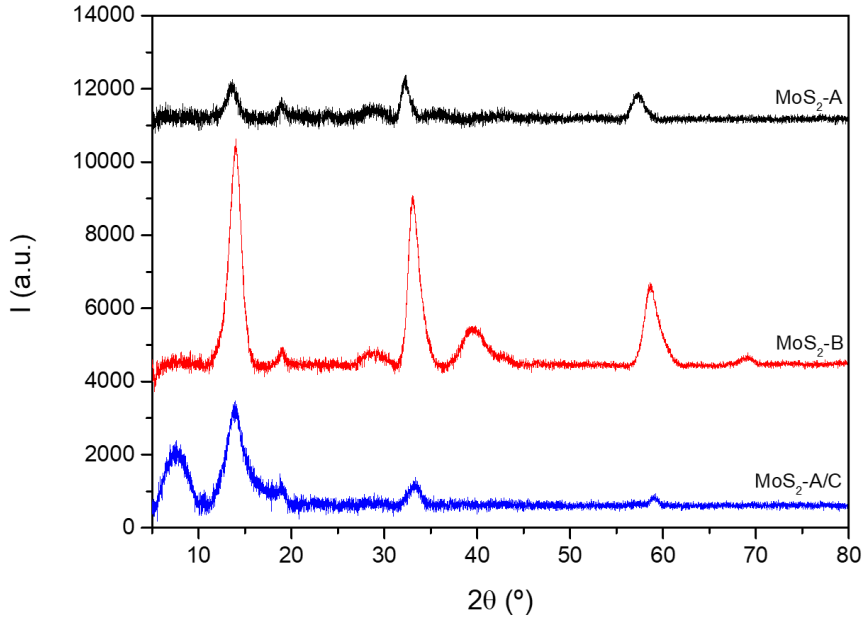

Figure 5. X-ray diffraction patterns of MoS_2-A (in black), MoS_2-B (in red) and MoS_2-A/C (in blue).

The sample morphology was examined by Scanning Electron Microscopy (SEM) (Carl Zeiss Ultra Plus). Figure 6 shows the SEM images of MoS_2-A (a) and MoS_2-A/C (b). The composition of the catalysts was determined by EDX as shown in Table 3. The MoS_2 black exhibits a Mo:S atomic ratio of approximately 1:2, close to the stoichiometry, confirming the successful formation of the MoS_2 phase and and in good agreement with the XRF results. In the case of the MoS_2-A/C, the atomic ratio is approximately 1:2.7, higher to stoichiometry for MoS_2. Based on that, the supported catalyst contains roughly 23.7 % wt. MoS_2 relative to the total active material.

Figure 7a and b show TEM images of the MoS_2-A/C sample, revealing the coexistence of particle aggregates and well-defined nanoparticles, the latter being more abundant. The particles are predominantly lamellar, rose-shaped, with sizes reaching several hundreds of nanometers. The observed morphology indicates a heterogeneous size distribution within the sample. Figure 7c depicts the particle size distribution histogram derived from quantitative analysis of particle dimensions measured across multiple TEM micrographs to ensure statistical representativeness. The mean particle size is determined to be 330 ± 110 nm.

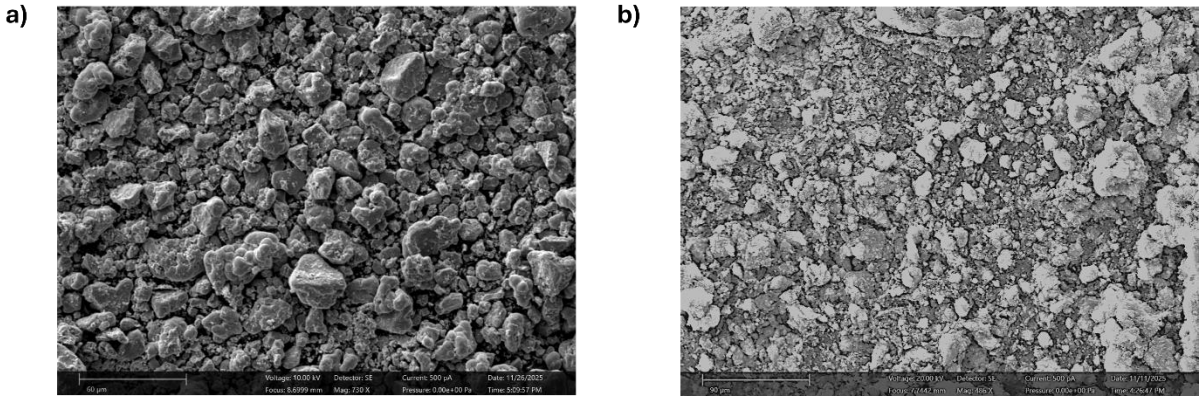

Figure 6. SEM images of MoS_2-A (a) and MoS_2-A/C (b).

Table 3. Elemental composition (% wt.) of MoS_2-A and MoS_2-A/C determined by EDX and XRF analyses

Sample	EDX (% wt.)			XRF (% wt.)		
	Mo	S	C	Mo	S	C
MoS_2-A	61.5	38.5	-	69.5	29.9	-
MoS_2-A/C	14.9	13.2	71.8	44.2	55.8	n.d.*

*n.d.: not detected, indicating that the element is below the detection limit of the technique.

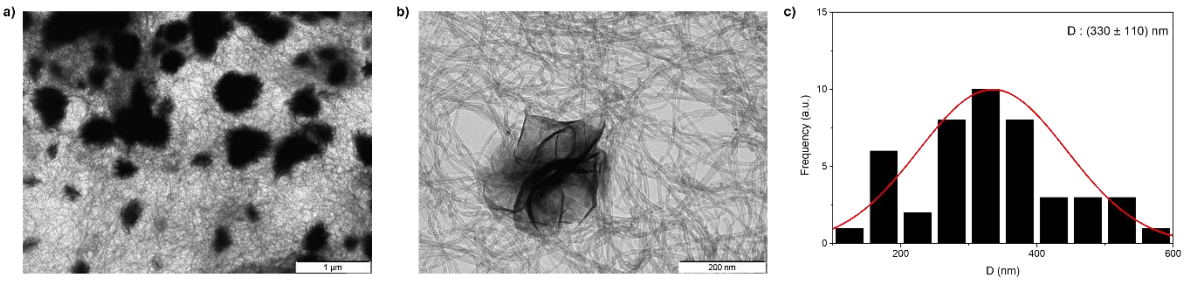

Figure 7. TEM image of MoS_2-A/C (a and b) and particle size distribution (c).

2.1.3 Nickel - Molybdenum disulfide (Ni-MoS_2)

Synthesis protocol (CIDETEC)

The Ni-MoS_2 catalyst was synthesized by a hydrothermal method. Specifically, molybdenum, nickel and sulphur precursors were each dissolved in ultrapure water and loaded into a Teflon-coated stainless-steel autoclave. The autoclave was placed in an oven, kept under static conditions at different temperatures (X and Y) for a specified period. Afterwards, the autoclave was removed from the oven and cooled to room temperature. The contents of the autoclave were then filtered under vacuum, recovering a black solid. The solid was washed using an ultrasonic bath, first twice with ethanol and then three times with UPW. Finally, the material was dried in an oven overnight.

Physicochemical characterization of obtained catalyst

The crystalline structure of the catalysts was confirmed by XRD as shown in Figure 8. Both samples prepared as Ni-MoS_2 exhibit a diffraction pattern characteristic of cubic NiS_2 (PDF#01-078-4702). Minor additional peaks are observed, attributed to residual precursors from incomplete reaction during synthesis. This observation indicates a higher tendency of nickel to form sulfides compared to molybdenum. No further characterization is performed at this stage, as current efforts are focused on optimizing the synthesis protocol to achieve effective doping of the MoS_2 lattice with nickel atoms.

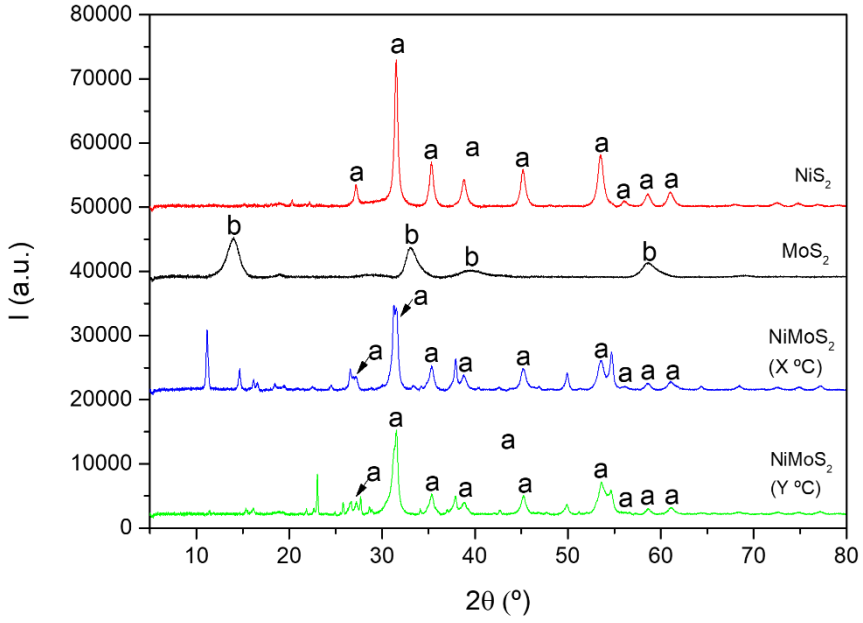

Figure 8. X-ray diffraction patterns of NiS_2 (in red), MoS_2 (in black) and Ni-MoS_2 synthesized at different temperatures: x (in blue) and y (in green).

2.1.4 Molybdenum carbide (Mo_2C)

Synthesis protocol (CIDETEC)

Protocol A: The Mo_2C/C supported catalyst was synthesized using NaCl as soft template. Specifically, NaCl templates and molybdenum and carbon precursors were dissolved in ultrapure water. The dispersion was dried overnight, then calcinated in inert atmosphere. The calcinated material was washed using ultrapure water and ethanol and finally dried in an oven overnight.

Protocol B: The Mo_2C/C supported catalyst was synthesized via a solid-solid reaction. Mixture of molybdenum and carbon precursors was combined with Ni precursor and KCl and processed in a ball mill for 30 min. The mixture was then calcinated under an inert atmosphere. Finally, the solid was washed with HCl and ultrapure water and dried overnight.

Physicochemical characterization of obtained catalyst

The crystalline structure of the catalysts was confirmed by X-ray diffraction (XRD), as shown in Figure 9. Both samples display a well-defined diffraction pattern characteristic of hexagonal Mo_2C. The main diffraction peaks appear at 2θ values of 34.3°, 37.9°, 39.3°, 52.1°, 61.5°, 69.5°, 74.6°, 75.5°, and corresponding to the (100), (002), (101), (102), (110), (103), (112), and (201) planes, respectively (PDF#00-035-0787). In addition to the main Mo_2C reflections, a small peak is observed at 26.5° in the sample prepared by Protocol B, attributed to residual Ni precursors, likely due to incomplete washing.

The crystallite size of Mo_2C in sample A is estimated at 21.1 nm using the Scherrer equation, with lattice parameters a = b = 3.0 Å and c = 4.9 Å, in agreement with theoretical values. For sample B, the crystallite size is estimated at 24.5 nm, with a = b = 3.0 Å and c = 4.96 Å.

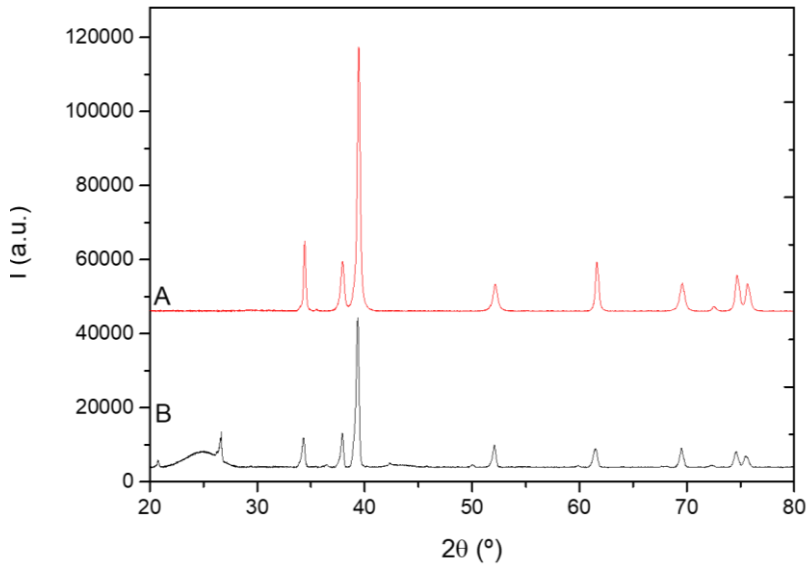

Figure 9. X-ray diffraction patterns of Mo_2C synthesized by protocol A (in red) and B (in black).

Figure 10 shows the SEM images of sample A (a) and B (b), highlighting the different morphologies resulting from the carburization conditions. With the protocol A (Figure 10a), the material exhibits highly dispersed Mo_2C domains forming nanofibrillar or needle-like structures, indicative of a mild or lower-temperature carburization process that minimizes sintering. In contrast, sample B (Figure 10b) shows a much more compact, granular surface composed of aggregated Mo_2C particles, characteristic of higher-temperature carburization. Together, the images demonstrate the strong influence of thermal treatment on the dispersion and crystallinity of Mo_2C materials.

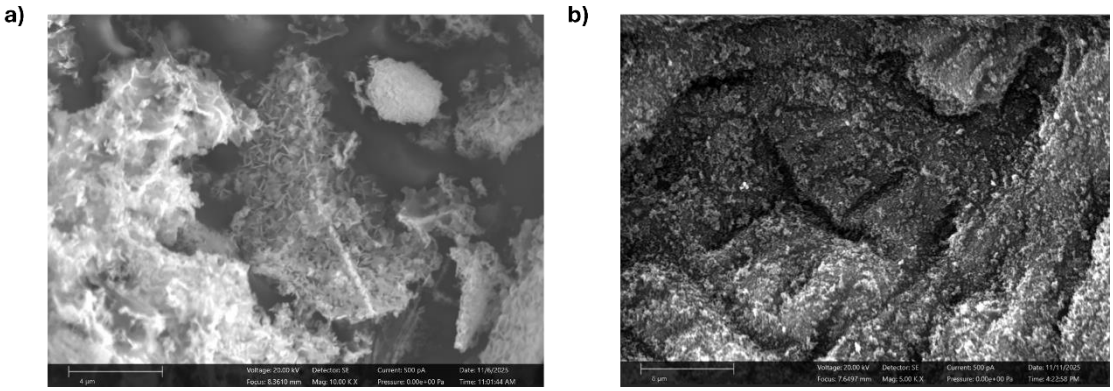

Figure 10. SEM images of Mo_2C/C synthesized by protocol A (a) and Mo_2C/C synthesized by protocol B (b).

The composition of the catalysts was determined using an Energy Dispersive X-ray (EDX) and are summarized in Table 4. Based on Mo:C atomic ratio of 2:1, the supported catalyst contains approximately 77.7 and 1.7 wt. % Mo_2C relative to the total active material for samples A and B, respectively. XRF was not used due to its limited sensitivity for carbon determination.

Table 4. Elemental composition (% wt.) of different Mo_2C samples determined by EDX analysis.

Sample	EDX (% wt.)	
	Mo	C
A	75.5	24.5
B	1.6	98.4

Figure 11a shows a TEM image of the Mo_2C/C – synthesized with protocol A. The image reveals rod-like Mo_2C nanostructures, consistent with the lamellar features previously observed in the SEM image (Figure 10a), anchored onto carbon sheets. The structures exhibit sizes reaching several hundred nanometres, indicating a heterogeneous size distribution within the sample. Figure 11b presents the particle size distribution, with an average size of 270 ± 90 nm. Overall, the TEM analysis confirms the successful formation of Mo_2C nanostructures anchored on carbon with good dispersion across the support.

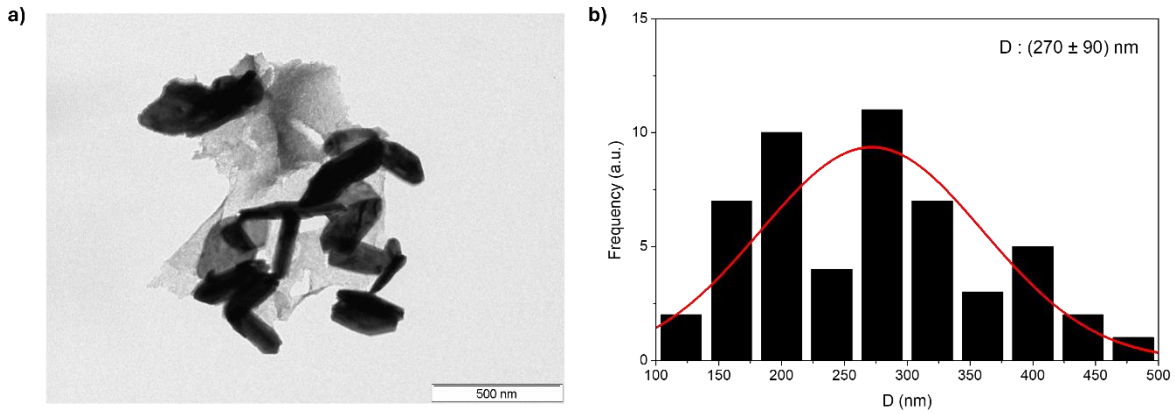

Figure 11. TEM image of Mo_2C/C-A (a) and particle size distribution (b).

2.1.5 Supported Nickel – Molybdenum (Ni-Mo/KB)

Synthesis protocol (CNR)

In the carbon supported synthesis, the precursors of Nickel Nitrate Hexahydrate ($Ni(NO_3)_2{\cdot}6H_2O$, Sigma Aldrich), Ammonium molybdate tetrahydrate ($(NH_4)_6Mo_7O_{24}{\cdot}4H_2O$, Sigma Aldrich) and Ketjenblack (KB) have been dissolved in ultrapure distilled water. At 60 °C, the solution was heated in a water bath and stirred. After the temperature reached, a hydroxide solution (1M, NaOH) was added gradually to achieve a pH value of 12. The solution kept under stirring at pH 12 and 60°C for 6 hours after that. The precipitate was then filtered and washed with hot ultrapure distilled water. The precipitate that was obtained was dried overnight at a temperature of 80°C. Finally, the precipitate obtained was reduced using 5 % hydrogen flow for a period of 6 hours at 550 °C.

Physicochemical characterization of obtained catalyst

The synthesized electrocatalysts have been characterized using a variety of techniques, including X-ray diffraction (XRD), X-ray fluorescence (XRF), Transmission electron microscopy (TEM) and Scanning electron microscopy (SEM).

For X-ray diffraction (XRD) analysis was used a D8 Advance diffractometer (Bruker AXS, Germany), operating with a Ni b-filtered Cu-Kα radiation (λ = 1.5406 Å) in the 2θ range 5–100° at 40 kV and 20 mA and a scan step of 0.03° s−1. To assess the crystalline phase of the catalysts developed, the XRD technique was utilized.

The supported NiMo/KB synthesized at pH value 12 is represented by the diffraction spectrum reported in Figure 12. The formation of a Ni:Mo alloy is confirmed by the characteristic bands of metallic Ni and a shift of diffraction peaks at lower angles in the electrocatalyst. Using the Scherrer formula, it was possible to determine an average crystallite size of 200 Å (22 nm).

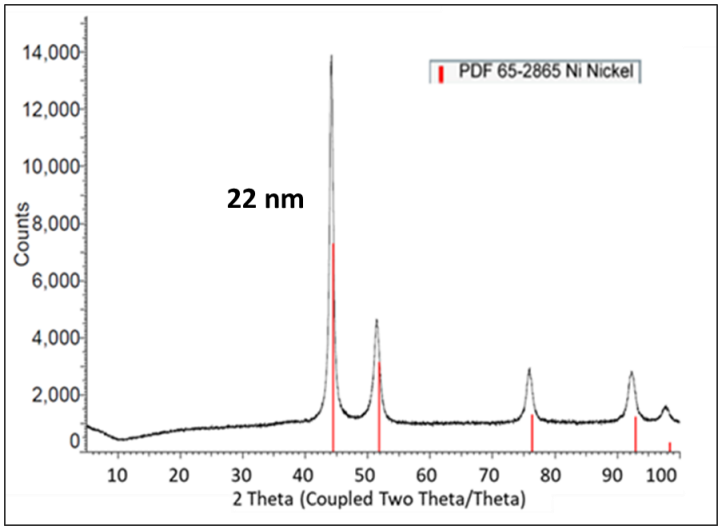

Figure 12. X-ray diffraction pattern of the cathodic catalyst synthesized NiMo/KB.

The catalyst's elemental composition was determined through X-ray fluorescence investigations (XRF), using a S8 TIGER spectrometer (Bruker AXS, Germany), equipped with a rhodium anode tube (power 4 kW and 75 µm Be window and LiF 220 crystal analyze).

The XRF analysis gives the opportunity to obtain semi-quantitative results on the atomic percentage of Ni:Mo alloys. The Table 5 shows the composition in weight percentage of NiMo/KB.

The electrocatalyst was characterized through scanning electron microscopy (SEM) and energy-dispersive X-ray (EDX) analysis using an SEM-FEG-UHR microscope (Thermo Fisher) equipped with a FIB (focused ion beam) column and STEM (scanning transmission electron microscopy) detectors. The instrument was operated at a voltage range of 2–15 kV, and the EDX probe was used to assess the bulk elemental composition of the samples.

Scanning electron micrographs of the NiMo/KB were reported in Figure 13a,b. Similar weight % of Ni and Mo was observed by SEM-EDX and XRF analysis (Table 5).

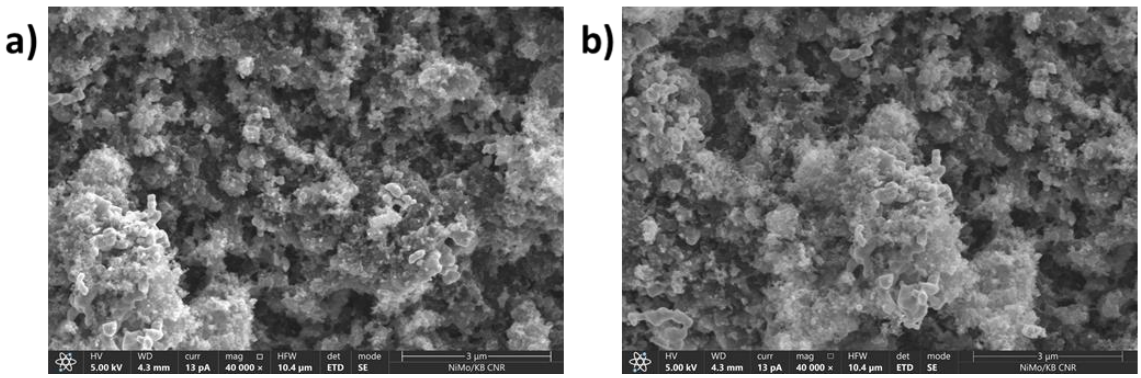

Figure 13. Scanning electron micrographs (a,b) of the cathodic catalyst synthesized NiMo/KB.

Table 5. Elemental composition (% wt.) of carbon supported cathode electrocatalysts determined by EDX and XRF analyses.

Sample	EDX (% wt.)		XRF (% wt.)	
	Ni	Mo	Ni	Mo
NiMo/KB	89.02	10.98	87.28	12.72

The electrocatalyst's morphology was studied with TEM using a JEOL JEM-F200 instrument equipped with an EDX spectrometer. The sample was prepared by ultrasonic dispersion of the catalyst in isopropyl alcohol and then depositing a drop of the suspension onto a holey carbon – coated Cu grid. The TEM images at different magnification of sample NiMo/KB synthesized were reported in Figure 14a-c. The morphology of the NiMo/KB catalyst showed a mixture of small circular and square-shaped particles.

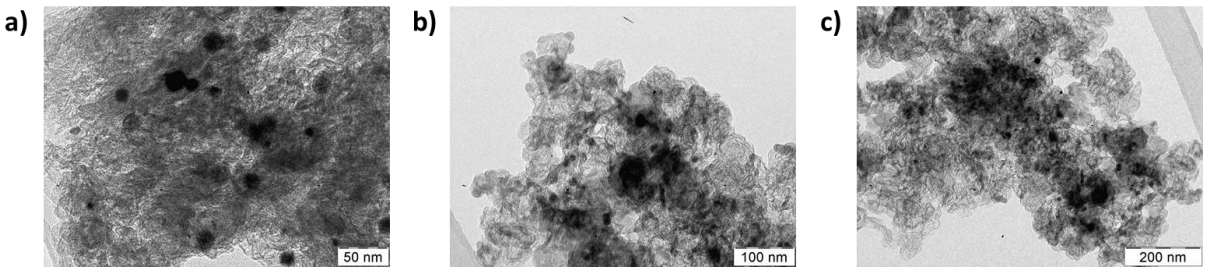

Figure 14. Transmission Electron Micrographs (a-c) of the cathodic catalyst synthesized NiMo/KB.

After optimizing the synthesis protocol, the next step was to scale up the NiMo/KB-based cathode catalyst. Supported NiMo/KB was synthesized in small and medium batches and characterized for maintaining good physicochemical properties, catalytic activity and stability achieved in small batches. The synthesis was increased (from 2g to 6g) using the same experimental procedure described previously, but with more reagents.

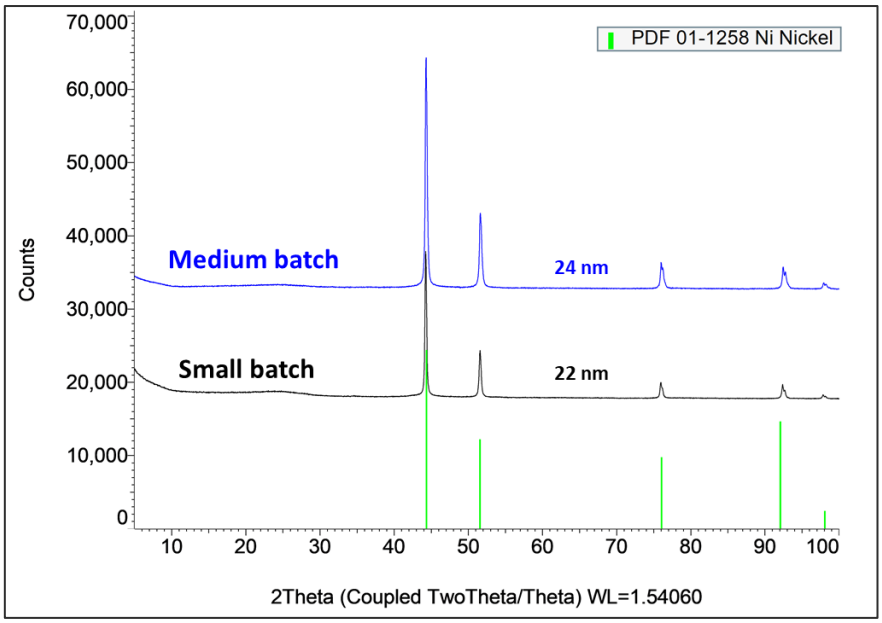

Figure 15. XRD patterns of the cathodic catalysts synthesized NiMo/KB.

To study the physicochemical properties of the synthesized electrocatalysts, different characterization techniques were used: X-ray diffraction (XRD) and X-ray fluorescence (XRF).

The XRD technique was employed to obtain the crystalline phases of the developed catalysts. The comparison of diffraction spectra between two batches synthesized (small and medium batches) is shown in Figure 15. The electrocatalysts are similar in their patterns, with characteristic bands of metallic Ni. A shift of diffraction peaks at lower angles in these two spectra confirms the formation of Ni:Mo alloy in all synthesized batches. It was possible to calculate, through the Scherrer formula, an average crystallite size of 220 Å (22 nm) for small batch and 240 Å (24 nm) for medium batch.

Table 6 shows the quantitative results on the weight percentage of the Ni:Mo alloys of the cathode electrocatalysts obtained with the XRF analysis.

Table 6. Elemental composition (% wt.) of different cathodic batches determined by XRF analysis.

NiMo/KB	Quantity (g)	Ni (% wt.)	Mo (% wt.)
Small batch	2 g	87.28	12.72
Medium batch	6 g	86.18	13.82

2.1.6 Pt/C – Benchmark cathode catalyst

The precious metal-based Pt/C (Platinum, nominally 40% on carbon black – Alfa Aesar) was performed as a commercial benchmark cathode to evolve hydrogen like in the conventional AEM electrolysis cell.

Physicochemical characterization of benchmark cathode catalyst (CNR)

The catalyst was characterized physicochemically through X-ray diffraction (XRD), Scanning electron microscopy (SEM) and Transmission electron microscopy (TEM).

For X-ray diffraction (XRD) analysis was used a D8 Advance diffractometer (Bruker AXS, Germany), operating with a Ni b-filtered Cu-Kα radiation (λ = 1.5406 Å) in the 2θ range 5–100° at 40 kV and 20 mA and a scan step of 0.03° s−1. XRD technique was used to examine the crystalline phase of the catalysts that were developed.

The average crystallite size was determined by X-ray diffraction and Figure 16 shows the diffraction pattern of commercial catalyst. Pt/C is characterized by the typical face-centred cubic (fcc) with diffraction peaks at 40°, 46.2°, 67.9°, 81.6° and 86° Bragg angles. The peaks are highly broadened with a crystallite size of 3.8 nm. It is possible to see the graphitic carbon at low Bragg angles (2θ ~25°).

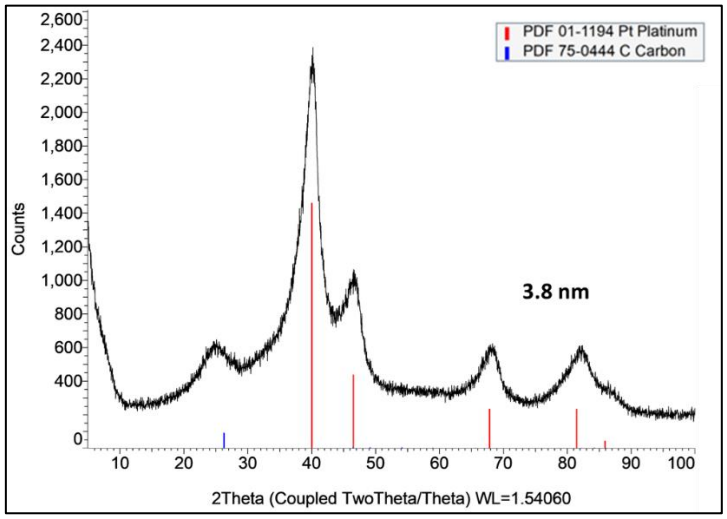

Figure 16. X-ray diffraction pattern of the commercial cathode catalyst Pt/C.

The benchmark cathode catalyst was characterized through scanning electron microscopy (SEM) and energy-dispersive X-ray (EDX) analysis using an SEM-FEG-UHR microscope (Thermo Fisher) equipped with a FIB (focused ion beam) column and STEM (scanning transmission electron microscopy) detectors. To determine the bulk elemental composition of the samples, the instrument was operated at 2–15 kV using the EDX probe.

Scanning electron micrographs of the commercial Pt/C were reported in Figure 17a-c. The weight percentage of Pt and C was observed by SEM-EDX analysis (Table 7).

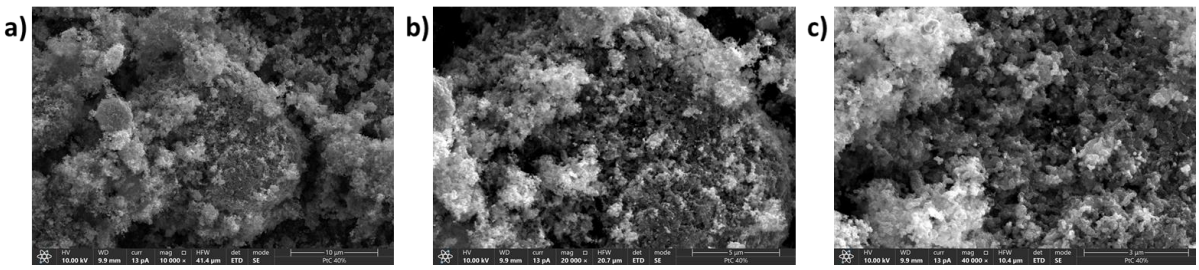

Figure 17. Scanning electron micrographs (a-c) of the commercial cathode catalyst Pt/C.

Table 7. Elemental composition (% wt.) of the commercial cathode catalyst Pt/C determined by EDX analysis.

Sample	EDX (% wt.)	
	Pt	C
40 % Pt/C	37.90	58.04

The morphology of the cathodic commercial electrocatalyst was investigated by TEM using a JEOL JEM-F200 instrument equipped with an EDX spectrometer. The sample was made by dissolving the catalyst in isopropyl alcohol using ultrasonic and depositing then a drop of the suspension on a holey carbon – coated Cu grid.

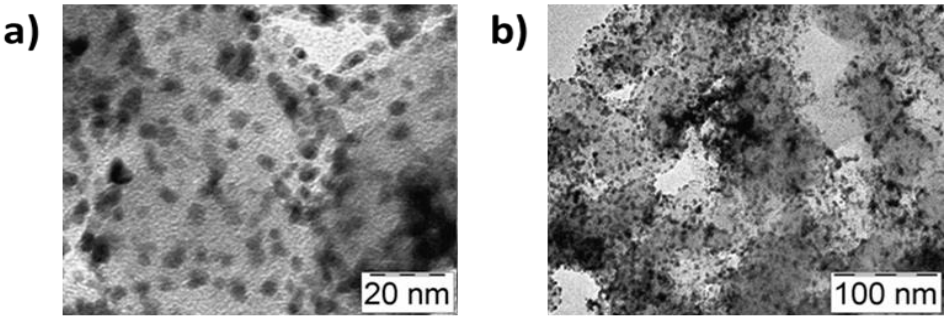

Figure 18. Transmission Electron Micrographs (a, b) of the commercial cathode catalyst Pt/C.

Figure 18a,b show the TEM images of carbon supported Pt/C benchmark cathode catalyst. The Pt/C catalyst displays very fine particles that are homogeneously dispersed over the carbon support.

2.2 PGM-free self-standing cathode electrocatalysts

PGM-free self-standing electrocatalysts refer to electrode materials that combine catalytic activity and mechanical integrity in a single, integrated structure. Unlike conventional metal powder catalysts, which are typically fabricated by depositing catalyst particles on a conductive substrate with the aid of polymeric binders (as described in previous sections), these self-standing electrodes can be directly formed on commercially available PTLs, resulting in strong adhesion between the active Ni–X alloy layer and the substrate. This configuration eliminates the need for additional binders or supports, thereby reducing interfacial resistance and improving electrical conductivity and long-term stability under harsh seawater conditions. The incorporation of secondary metals (X = Fe, Co, Mo, Cu, etc.) into the Ni matrix further enhances catalytic activity, corrosion resistance, and bubble release dynamics. Overall, such PGM-free, self-standing Ni–X alloy electrodes provide a cost-effective and durable alternative to platinum-based cathodes, aligning with the goals of sustainable and large-scale hydrogen production from seawater.

2.2.1 Binary Nickel-based alloy (Ni-X, X = Mo)

Electrodeposition process and characterization (CIDETEC)

Self-standing Ni–Mo electrodes were fabricated by electrodeposition from an aqueous electrolyte containing nickel and molybdenum salts as metal precursors, together with an organic complexing agent to enable induced co-deposition of the alloy. The initial screening of electrodeposition parameters was performed using a Hull Cell configuration - small test cell used in electrodeposition to evaluate and optimize plating baths (Figure 19a). Its angled cathode creates a continuous range of current densities, allowing a single short test to show how deposit appearance and quality change across that range. This helps identify the optimal current density, electrolyte pH, and temperature on the deposit composition and morphology, as well as troubleshoot plating issues before scaling up to full production.

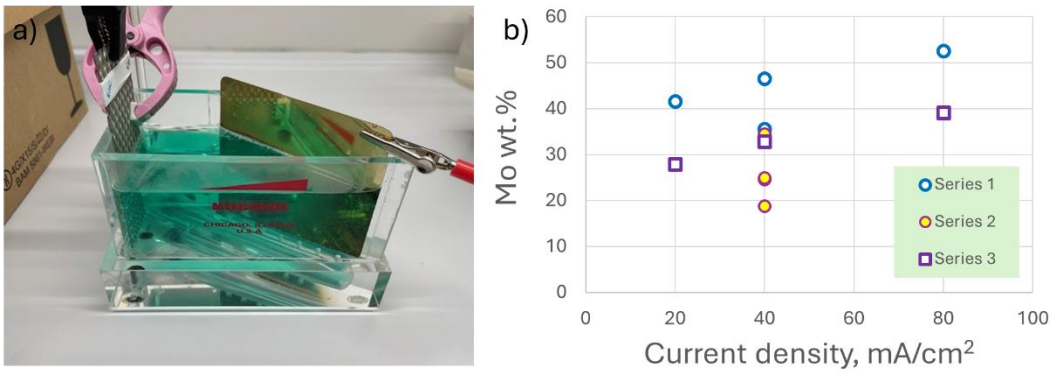

Figure 19. (a) Photo of Hull Cell test used at CIDETEC to screen electrodeposition conditions for Ni-Mo alloy. (b) Composition of Ni-Mo alloy determined by EDX analysis after extrapolating the Hull Cell results to electrodeposition on flat Cu disk substrates.

Based on the optimal conditions identified in the Hull cell, the process was subsequently scaled up to a 1 L glass beaker setup for electrodeposition on flat Cu substrates. The results indicate that the Mo content in the deposits can be tuned between approximately 20 and 50 wt.% by adjusting the electrodeposition conditions (Figure 19b). Figure 20 shows the variation in surface morphology and composition of the resulting Ni–Mo coatings. The surface morphology of electrodeposited Ni-Mo alloys reveals a pronounced dependence on both current density and electrodeposition temperature, as demonstrated in the provided SEM micrographs. At lower current densities (20 and 40 mA/cm²), the deposits display large, relatively coalesced granules with a compact structure, suggesting slower nucleation and growth rates that favour grain agglomeration. With a further increase in current density to 80 mA/cm² (Figure 20c), the alloy surface transitions to a finer, more fragmented granular morphology, characterized by densely packed nodules and a higher degree of surface roughness, indicative of enhanced nucleation events and faster metal ion reduction. Variations in the electrodeposition temperature also significantly affect the grain structure that changes from granular (at 50 °C) to isolated nodules within a smoother matrix at higher temperatures, as seen in Figure 20d-f.

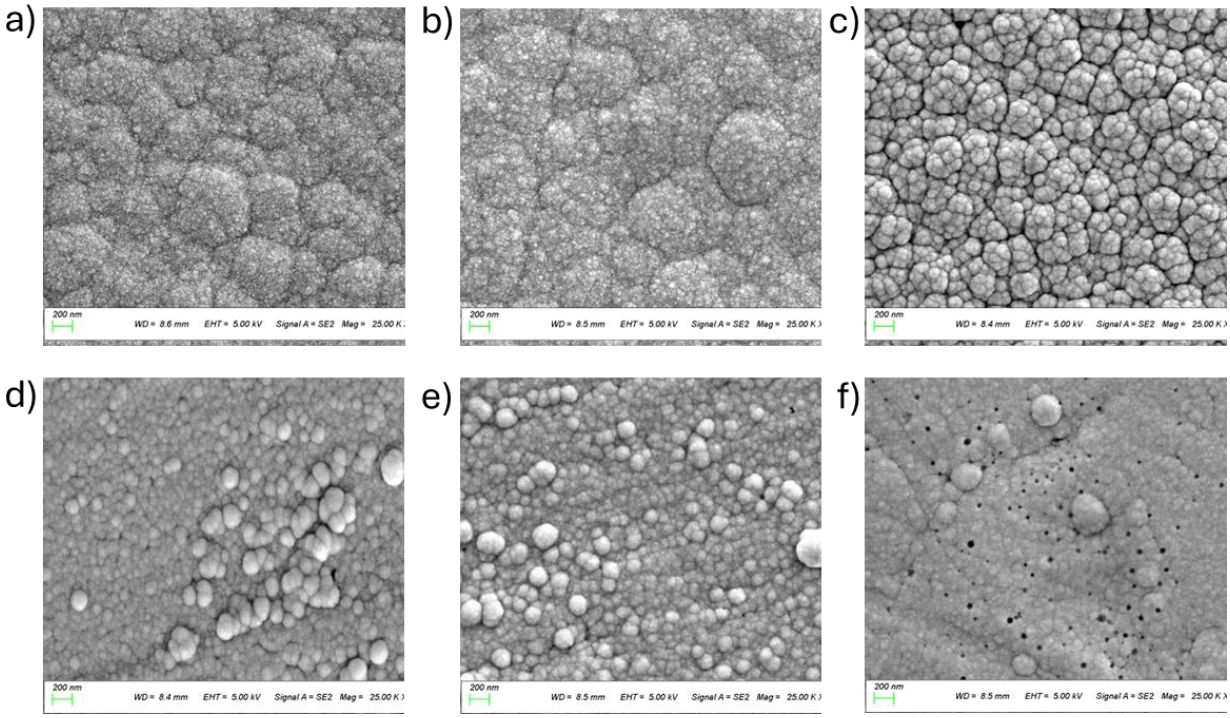

Figure 20. Surface morphology of electrodeposited Ni-Mo alloys. Effect of current density: (a) 20 mA/cm², (b) 40 mA/cm², (c) 80 mA/cm². Effect of electrodeposition temperature: (d) 50 °C, (e) 60 °C, and (f) 70 °C.

X-ray diffraction (XRD) analysis (Figure 21) revealed only the characteristic peaks of the Cu substrate, along with a broad shoulder around 44°, which is attributed to the formation of an amorphous-like Ni–Mo solid solution. The absence of a distinct Ni or Ni-Mo peak at 20 and 40 mA/cm² in the XRD patterns can be attributed to the limited crystallinity and/or very thin deposit of the alloy at these lower current densities. At such conditions, nucleation rates are lower, leading to the formation of either amorphous or nanocrystalline phases with small grain sizes, which result in broadened and less intense XRD peaks that are often indistinguishable from the background or overshadowed by the strong substrate peaks. Indeed, at such Mo concentrations, the formation of amorphous solid solution is expected.

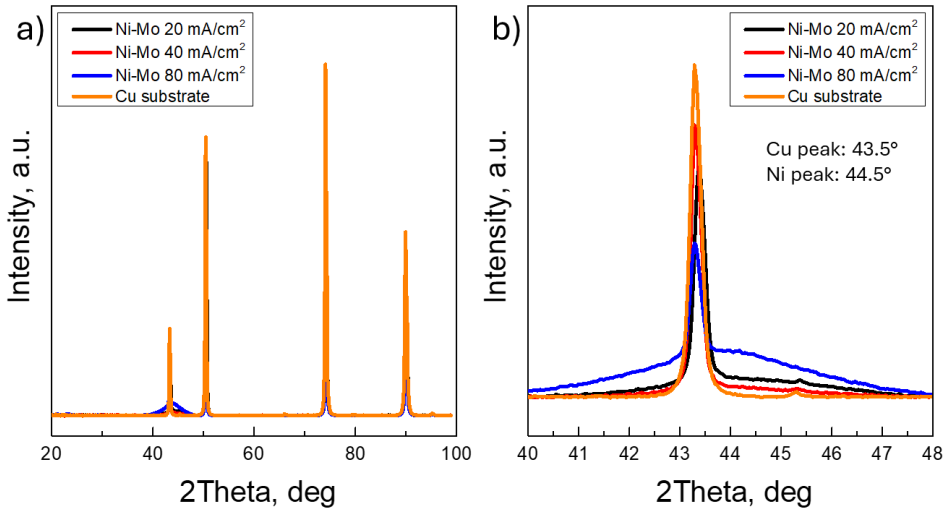

Figure 21. X-Ray diffraction patterns of Ni-Mo alloys electrodeposited onto flat Cu disks: (a) full spectra and (b) zoom around the main Cu and Ni peaks.

Following the optimization on flat substrates, Ni–Mo alloys were electrodeposited onto a Ni felt substrate to produce self-standing, three-dimensional electrodes. As shown in Figure 22, the Ni–Mo coating retained a similar morphology and composition despite the complex 3D geometry of the substrate.

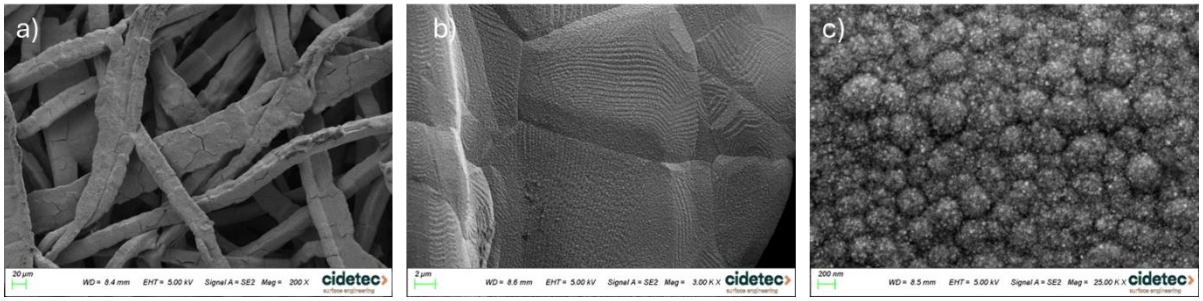

Figure 22. Surface morphology of Ni-Mo alloy electrodeposited on Ni felt fibers: (a) low magnification image showing the fiber structure, (b) higher magnification image showing the Ni-Mo coated singe fiber where the coating replicates the grain structure of the Ni felt, and (c) high resolution image demonstrating the details of the Ni-Mo characteristic morphological features.

2.2.2 Ternary Nickel-X-Y alloy (Ni-X-Y, X=Mo, Y=S)

Electrodeposition process and characterization (CIDETEC)

Incorporating sulphur into Ni–Mo alloys is an approach to enhance the catalytic performance of the catalyst, particularly for HER alkaline and seawater electrolysis. While S incorporation into Ni–Mo catalysts has been shown to improve HER performance, the direct electrodeposition of Ni–Mo–S alloys is less standardized approach compared to conventional post-treatment methods.

Similarly to the Ni–Mo electrodeposition, the preliminary screening of the Ni–Mo–S system was carried out using a Hull cell configuration. In addition to current density, temperature, and pH, two sulphur sources, i.e. thiourea and sodium thiosulfate, were evaluated. Remarkably, in both cases, the presence of sulphur-containing species in the electrolyte significantly suppressed Mo co-deposition. As a result, alloys containing up to approximately 8 % wt. S (thiourea) and 12 % wt. S (thiosulfate) were obtained, while the Mo content consistently remained below 1 wt.% regardless of the applied current density. This behaviour is likely associated with the strong adsorption of sulphur species on the cathode surface, which can hinder Mo reduction, as well as shift the equilibrium distribution of complex metal ions in the electrolyte induced by sulphur-containing components. It should also be noted that accurate quantification of the Mo:S ratio in the Ni–Mo–S alloys is challenging due to the close overlap of the Mo and S peaks in the EDX spectra, as illustrated in Figure 24.

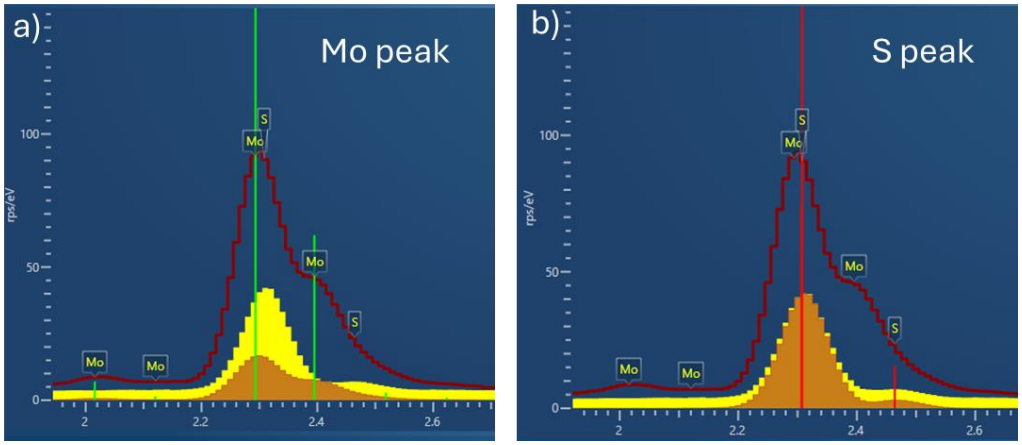

Figure 23. EDX peak position of Mo (a) and S (b). The main Mo and S peaks are close together and show appreciable overlap in energy position.

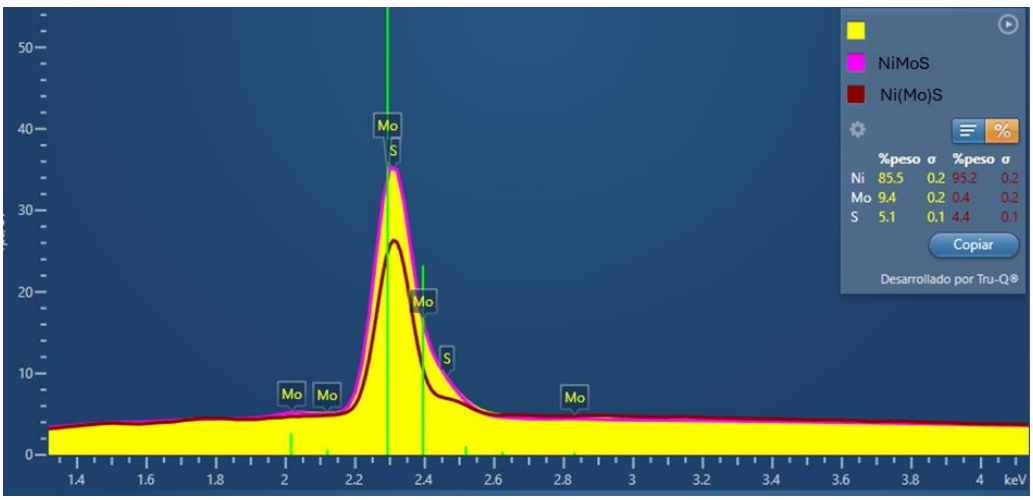

Figure 24. EDX spectra of Ni-Mo-S and Ni-(Mo)-S catalysts where the Ni:Mo:S ratio was changed by adjusting electrodeposition conditions.

The Ni:Mo:S ratio in a catalyst is critically important for optimizing its performance in the HER. A decrease in the Mo content in the Ni-Mo-S catalyst due to S incorporation can affect the balance of catalytic function since Mo sites are crucial for active hydrogen evolution in the Ni-Mo system. A lower Mo content may reduce the number of effective catalytic sites responsible for HER. However,

moderate sulphur incorporation often results in a structural change where sulphur is integrated into the lattice, which can still maintain or even enhance activity by improving intrinsic site properties. Excessive sulphur beyond an optimum level can cause formation of MoS_2 islands or segregates that might have lower HER activity than S-doped Ni-Mo alloys. Therefore, the beneficial effect of sulphur depends on achieving an optimum balance between S doping and Mo content to maximize active site availability and catalytic efficiency. To promote Mo incorporation along with S, the bath composition was modified leading to up to 9 % wt. Mo co-deposited along with 5 % wt. of S, as shown in Figure 23.

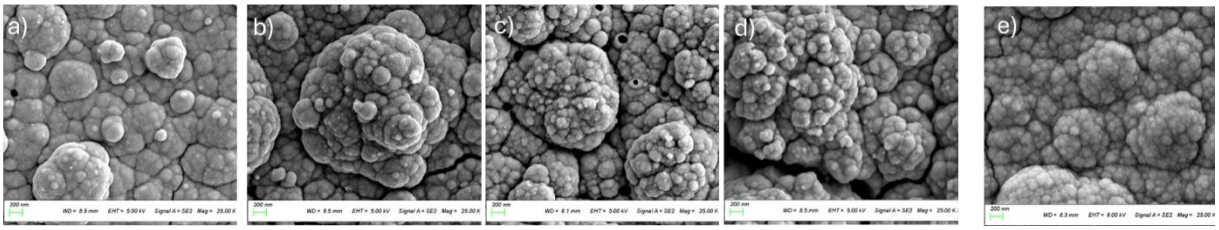

Figure 26. Surface morphology of NiMoS electrocatalysts at different deposition current densities. (a–d) Representative Ni(Mo)S samples obtained at (a) 10 mA/cm², (b) 20 mA/cm², (c) 40 mA/cm², and (d) 80 mA/cm², illustrating increasing particle size and aggregation with higher current. Panel (e) shows the surface of representative Ni-Mo-S sample, displaying more uniform and fine-grained clusters associated with higher Mo incorporation.

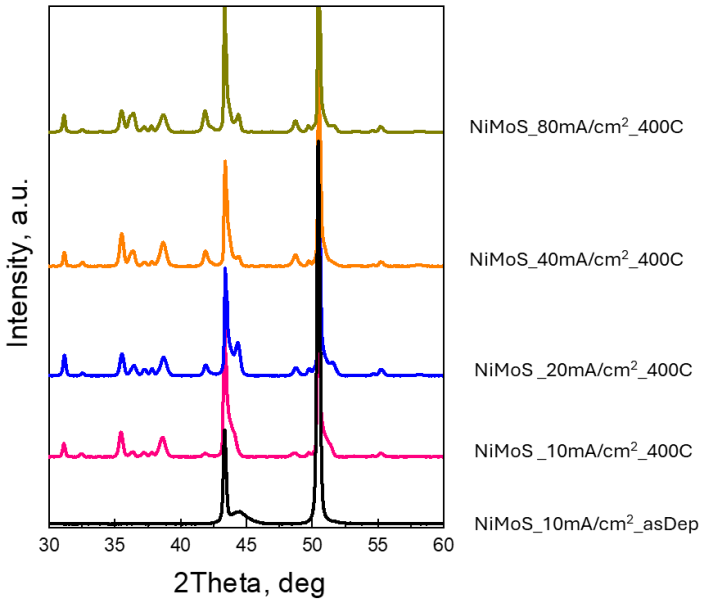

Figure 25. XRD patterns of NiMoS alloy films deposited on copper substrates at current densities of 10, 20, 40, and 80 mA/cm², shown before (as-deposited, black curve) and after heat treatment in air at 400°C for 2h in air atmosphere.

Figure 26 shows the representative surface morphology images of NiMoS electrocatalysts synthesized under varying deposition current densities. Images (a) through (d) illustrate that increasing the current density from 10 mA/cm² to 80 mA/cm² results in a noticeable transition in grain size, surface roughness and granular aggregation. At low current density (a), the deposit consists of relatively small, packed spherical particles. As the current density increases (b, c, d), particles become much larger and the surface grows more textured, suggesting greater nucleation. Image (e) depicts the Ni-Mo-S catalyst, where Mo content is increased up to 9 % wt. The surface is characterized by finer and more uniformly distributed clusters, indicating the effect of Mo addition on deposit structure.

The crystallographic structure of the Ni–Mo–S deposits was examined by XRD, Figure 25. Similarly to the Ni–Mo alloys, the two strong sharp peaks near 43.5° and 50.5° 2θ are characteristic of Cu, which is the substrate and thus dominates the pattern. Peaks at lower intensities (33–40° and 56–58°) may correspond to poorly crystalline or amorphous Ni-Mo or Ni-Mo-S phases, but are partially masked by the dominant Cu substrate peaks. No clear peaks for crystalline MoS_2, NiS, or NiO/oxides are evident, suggesting primarily amorphous Ni-Mo-S alloy in the as-deposited state. Annealing is a common strategy for post-treatment of S-containing electrodeposited materials which helps to eliminate the excess of S and form active crystallographic phases. In this case, the heat treatment was performed at 400 °C for 2 h in air (to further promote Mo oxide formation for increased HER activity).

After heat treatment, there is a notable increase in peak definition and higher peak intensity in the regions near the Cu peaks, especially as current density increases. Secondary peaks (33–40°, 56–58° 2θ) become more pronounced, which likely represent formation of crystalline phases such as NiO, MoO_3, or $NiMoO_4$ after oxidation in air. Weak but sharper peaks may correspond to NiO (typically at 37.3°, 43.3°), MoO_3, $NiMoO_4$, and/or sulfide species, however, their assignment is not straightforward. No high-intensity peaks for MoS_2 (typically at 33.2°, 58.5° for 2H MoS_2) are observed, supporting conversion to oxides rather than formation of sulfides post-heat treatment, yet it is worth noting that the S content was preserved after the heat treatment. The Cu substrate peaks remain dominant across all samples (43.3°, 50.4°), but minor alloy or oxide phases show increased crystallinity with higher deposition current and thermal treatment.

Subsequently, the Ni–Mo–S alloys were electrodeposited onto Ni felt substrates to produce self-standing electrodes. As shown in Figure 27, the surface morphology and composition of the alloys were well preserved on the three-dimensional substrate. However, the adhesion of the coating appears to be compromised, which may result from lattice mismatch between the deposit and the Ni substrate, interference from the S-species adsorption on the substrate, or from insufficient surface activation prior to electrodeposition.

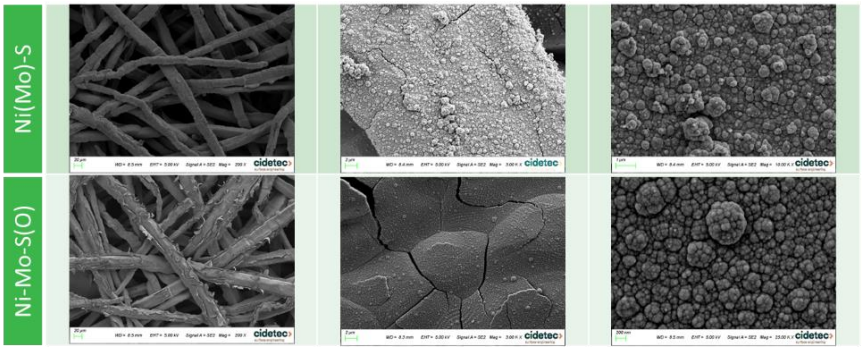

Figure 27. Surface morphology of Ni-Mo-S electrocatalysts deposited onto the Ni felt. The images are taken at different magnifications to depict the fiber structure, individual fiber coverage and the details of the coating morphology covering the fibers.

3 Oxygen evolution electrocatalysts

Within the SWEETHY project, the development of PGM-free metal catalysts for the anode has focused on the synthesis of nanosized (<10 nm) non-CRM metal oxides, primarily Ni-Fe and Ni-Mn based systems, aimed at producing spinel structures and Layered Double Hydroxides (LDH) as promising candidates for anode catalysis. Among these, NiFe oxides constitute the core materials under investigation. LDH-type catalysts combine favourable electrical conductivity with high oxygen-evolution activity; however, their long-term stability under seawater electrolysis conditions remains a significant challenge. To address this, targeted thermal treatments and chemical modifications will be applied to enhance their durability and overall performance in saline environments.

3.1 PGM-free metal powder anode electrocatalysts

3.1.1 Nickel-Iron Layered Double Hydroxide (NiFe-LDH)

Nickel-Iron Layered Double Hydroxide were synthesized at both CIDETEC and CNR.

Synthesis protocol (CIDETEC)

Protocol A: The NiFe-LDH catalyst was synthesized by a coprecipitation method. Specifically, a nickel and iron precursors, along with a compound containing the desired interlayer anion, were dissolved in acidic ultrapure water. Once fully dissolved, a base solution was added dropwise until a target pH was reached. The resulting solution was stirred for 24 h to complete the precipitation process. The solid was then filtered under vacuum, recovering a brown-green solid. The solid was washed using an ultrasonic bath, first three times with UWP and then twice with ethanol and finally dried overnight.

Protocol B: The NiFe-LDH catalyst was synthesized by a hydrothermal method. Nickel and iron precursors, along with a base, were dissolved in two different solvents (solvent 1 = sample B.1, and solvent 2 = sample B.2) and loaded into a Teflon-coated stainless-steel autoclave. The autoclave was placed in an oven, kept under static conditions at the desired temperature for a specified period. Afterwards, the autoclave was removed from the oven and cooled to room temperature. The contents of the autoclave were then filtered under vacuum, recovering a brown solid. The solid was washed using an ultrasonic bath, first three times with UWP and then twice with ethanol. Finally, the material was dried in an oven overnight.

Physicochemical characterization of obtained catalyst at CIDETEC

On the one hand, the results obtained using Protocol A demonstrate the crystalline structure of the NiFe-LDH catalysts, which is confirmed by X-ray diffraction (XRD), as shown in Figure 28. The diffractograms clearly reveal the characteristic reflections of the hexagonal LDH phase, with peaks at 11.4°, 22.8°, 34.3°, 38.3°, 38.7°, 45.9°, 59.5°, and 60.7°, corresponding to the (003), (006), (009), (012), (018), (110), and (113) planes, respectively. The measured lattice parameters and crystallite sizes for different intercalated anions are summarized in Table 8.

Crystallite sizes, calculated using the Scherrer equation, range from 3.8 nm to 5.0 nm, confirming that the synthesis method consistently produces nanometric materials. These results align with the target

particle size for this project, which aims to maximize surface area and accessibility of active sites by keeping the LDH domains in the nanometer range.

Regarding anion exchange, the a and b lattice parameters remain nearly constant, ranging from 3.08 Å to 3.09 Å, reflecting the stability of the in-plane metal cation arrangement regardless of the interlayer anion. Analysis of the c-axis parameter and d(003) spacing further suggests that CO_3^{2-} could be preferentially incorporated under standard synthesis conditions, as indicated by minimal differences between d(003) and c values. Modifying the interlayer anion could tune structural and electrochemical properties. Consequently, ongoing work focuses on adjusting the synthesis conditions and exploring alternative anions to enhance the electrochemical performance of NiFe-LDH catalysts while maintaining nanometric crystallite dimensions.

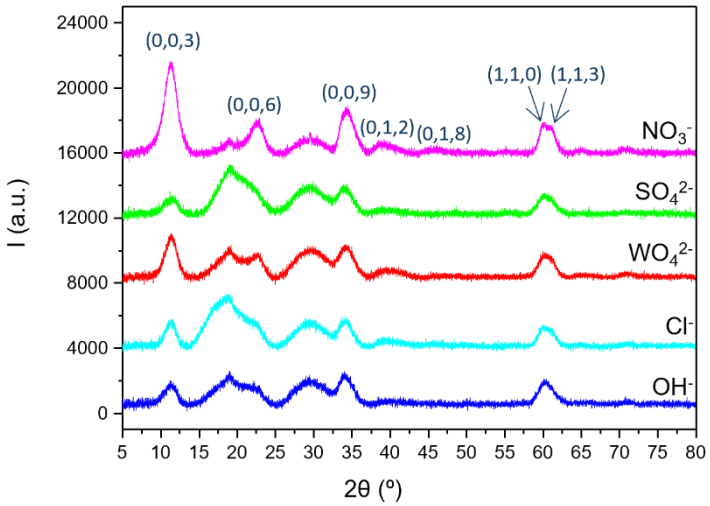

Figure 28. X-ray diffraction patterns of Ni-Fe LDH materials synthesized via protocol A.

Table 8. Cell parameters, d(003) spacing and crystallite size for different Ni-Fe LDH materials synthesized via protocol A.

Anion	a=b (Å)	c (Å)	d (003) (Å)	Crystallite size (nm)
NO_3^-	3.08	23.51	7.84	4.1
SO_4^{2-}	3.09	23.53	7.84	3.8
WO_4^{2-}	3.08	23.42	7.81	4.1
Cl^-	3.09	23.55	7.85	5.0
OH^-	3.08	23.68	7.89	4.2

On the other hand, XRD analysis of the materials obtained via Protocol B.1 (Figure 29, in red) reveals well-defined reflections of the hexagonal LDH phase, with peaks at 11.2°, 22.7°, 34.3°, 38.7°, 45.8°,

59.8°, and 61.1°, corresponding to the (003), (006), (009), (012), (110), and (113) planes, respectively. The in-plane lattice parameters a = b are approximately 3.1 Å, while the c parameter is 23.6 Å. Crystallite sizes, calculated using the Scherrer equation is 13.9 nm, confirming the formation of nanometric domains. These values are consistent with CO_3^{2-} intercalation under conventional hydrothermal conditions.

In contrast, materials obtained via Protocol B.2 (Figure 29, in black) exhibit XRD peaks at slightly higher angles (33.2°, 38.7°, 52.1°, 59.4°, and 62.8°), with smaller crystallite sizes around 7 nm. The a and b lattice parameters remain nearly constant (≈3.1 Å), while the c parameter increases to ~24.2 Å. The expansion of the interlayer spacing suggests preferential incorporation of NO_3^- anions instead of CO_3^{2-}. This larger interlayer distance may facilitate ion diffusion, which is advantageous for subsequent anion exchange processes, such as substitution with WO_4^{2-} or SO_4^{2-}. However, the relatively low crystallinity observed in B.2 introduces some uncertainty in the XRD-derived parameters, making this observation preliminary. Consequently, ongoing efforts focus on improving crystallinity using Protocol B.2, which appears most suitable for controlled anion exchange while maintaining nanometric LDH domains.

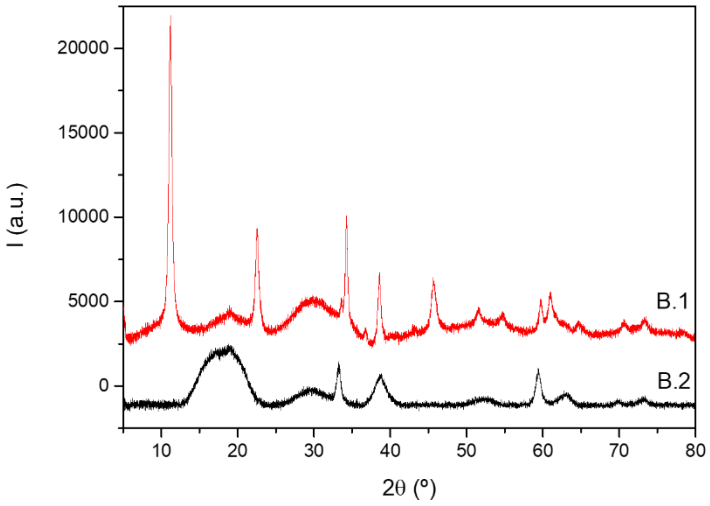

Figure 29. X-ray diffraction patterns of Ni-Fe LDH materials synthesized via protocol B.1 and B.2.

Focusing on the sample synthesized via protocol B.1, which exhibits a well-defined crystalline structure, its composition was measured by EDX and XRF. Both techniques yielded similar results, indicating a Ni:Fe ratio close to 1:2 (Table 9). TEM analysis was then performed to correlate these compositional results with the morphology of the sample at the nanoscale. In Figure 30a, quasi-spherical nanoparticles are observed, and individual particles can be clearly distinguished despite partial clustering. Figure 30b presents the corresponding particle size distribution, obtained from statistical analysis of a representative number of particles. The histogram follows an approximately Gaussian profile, with a mean diameter of 7 ± 2 nm, centered around 7 nm. The relatively narrow distribution indicates good control over the synthesis conditions, although some degree of

agglomeration is evident. Overall, the TEM analysis confirms the successful formation of nanoscale Ni–Fe LDH particles with a fairly uniform size distribution.

Table 9. Elemental composition (% wt.) of the NiFe LDH determined by EDX and XRF analyses.

EDX (% wt.)		XRF (% wt.)	
Ni	Fe	Ni	Fe
60.0	40.0	70.2	29.8

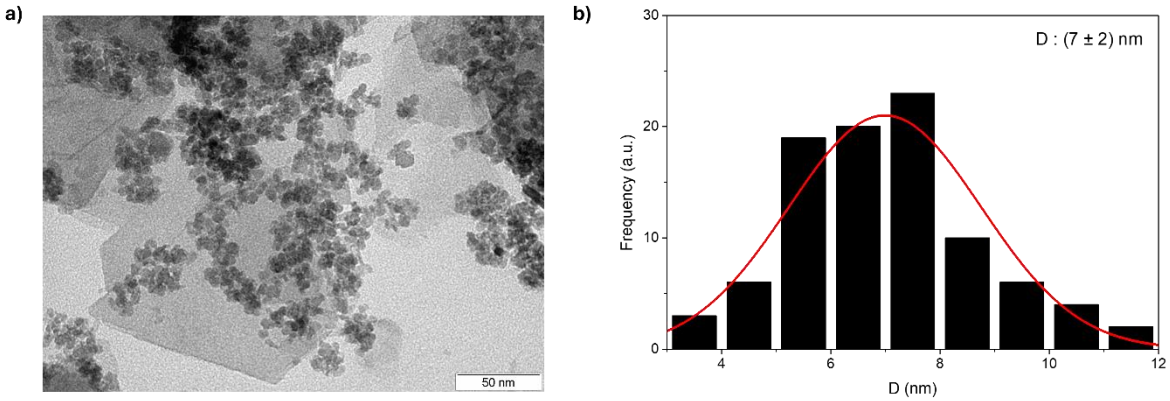

Figure 30. TEM image of Ni-Fe LDH synthesized via protocol B.1 (a) and particle size distribution (b).

Synthesis protocol (CNR)

The anode catalyst was prepared using the co-precipitation method. The precursors based on Iron Nitrate Nonahydrate ($Fe(NO3)_3 \cdot 9H_2O$, Sigma Aldrich) and Nickel Nitrate Hexahydrate ($Ni(NO_3)_2 \cdot 6H_2O$, Sigma Aldrich) have been dissolved in ultrapure distilled water. The solution was immersed in a hot water bath and stirred at 60 degrees Celsius. After reaching the desired temperature, a hydroxide solution (1M, NaOH) was added slowly to achieve a pH of 9. Subsequently, the suspension was stirred at pH 9 and 60 °C for 4 h. At the conclusion of this period, the precipitate was filtered, washed with hot ultrapure distilled water. The precipitate obtained was dried at 80 °C overnight and subsequently sieved.

Physicochemical characterization of obtained catalyst at CNR

To investigate the physicochemical characteristics of the synthesized electrocatalysts, different characterization techniques have been performed: XRD, XRF, SEM/EDX and TEM.

For X-ray diffraction (XRD) analysis was used a D8 Advance diffractometer (Bruker AXS, Germany), operating with a Ni b-filtered Cu-Kα radiation (λ = 1.5406 Å) in the 2θ range 5–100° at 40 kV and 20 mA and a scan step of 0.03° s−1. Using the XRD technique, the crystalline phase of the developed catalysts was assessed.

The XRD pattern reported in Figure 31 shows the diffraction spectrum of Nickel-Iron Layered Double Hydroxide (NiFe-LDH) catalyst synthesized. The XRD spectrum is associate to three structures: $Ni(OH)_2$, $Ni(OH)_2 \cdot 0.75H_2O$ and FeO(OH). The combination of fine crystallite size and larger crystallite size results in broad peaks and narrower peaks. The Scherrer formula was utilized to determine an average crystallite size of 46.3 Å (4.6 nm).

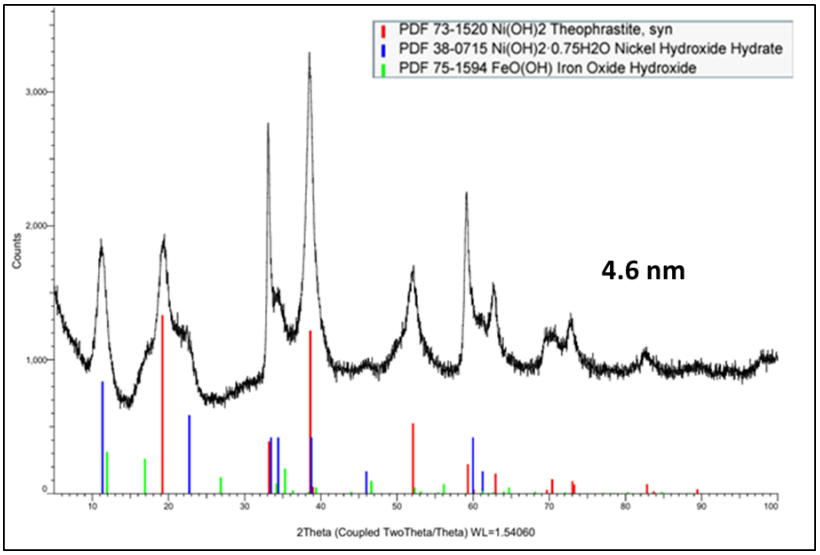

Figure 31. XRD patterns of the anodic catalyst synthesized NiFe oxide-hydroxide.

The S8 TIGER spectrometer (Bruker AXS, Germany), equipped with a rhodium anode tube (power 4 kW and 75 µm Be window and LiF 220 crystal analyze) was used to determine the elemental composition of the catalyst through X-ray fluorescence investigations (XRF). By using XRF, semi-quantitative results on the atomic ratio of Ni:Fe oxide-hydroxide could be obtained.

The anodic catalyst synthesized NiFe was characterized through scanning electron microscopy (SEM) and energy-dispersive X-ray (EDX) analysis using an SEM-FEG-UHR microscope (Thermo Fisher) equipped with a FIB (focused ion beam) column and STEM (scanning transmission electron microscopy) detectors. The instrument was operated in the range 2–15 kV, and the EDX probe was used to determine the bulk elemental composition of the samples.

The morphology and composition of NiFe oxide-hydroxide were examined by SEM and SEM/EDX. Figure 32a,b reports some representative SEM images of the NiFe catalyst investigated. Large agglomerates of small particles are formed, as proven by higher magnification images (Figure 32b).

The elemental composition analysis by SEM/EDX confirm the atomic %wt. of Ni and Fe obtained by XRF analysis. The results from both techniques are reported in Table 10.

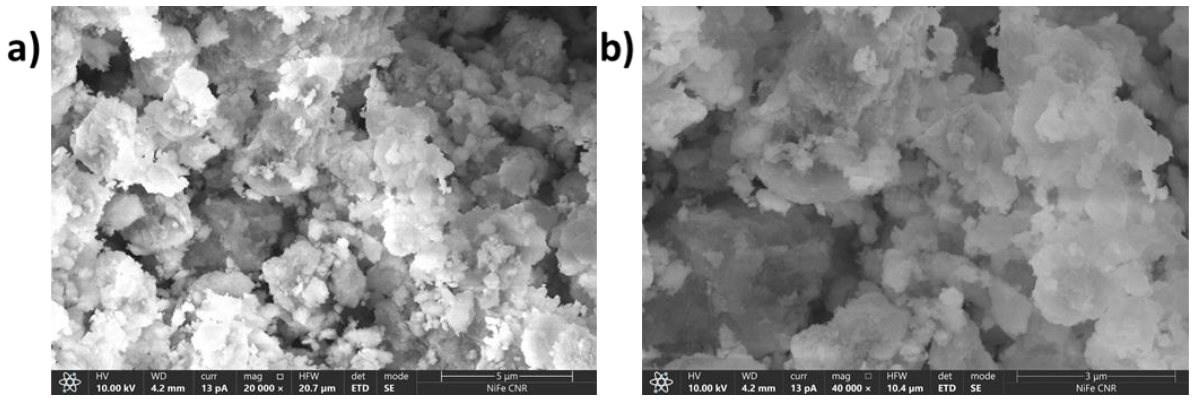

Figure 32. Scanning Electron Micrographs (a,b) of the synthesized anodic catalyst NiFe (LDH).

Table 10. Elemental composition (% wt.) of anodic electrocatalyst determined by EDX and XRF analyses.

Sample	EDX (% wt.)		XRF (% wt.)	
	Ni	Fe	Ni	Fe
NiFe LDH	83.13	16.87	85.24	14.74

For the synthesized NiFe LDH, both the EDX and XRF results are in good agreement, suggesting a Ni:Fe ratio close to the predetermined stoichiometry.

The morphology of the electrocatalyst was examined by TEM using a JEOL JEM-F200 instrument equipped with an EDX spectrometer. The sample was made by dissolving the catalyst in isopropyl alcohol using ultrasonic and depositing then a drop of the suspension on a holey carbon – coated Cu grid.

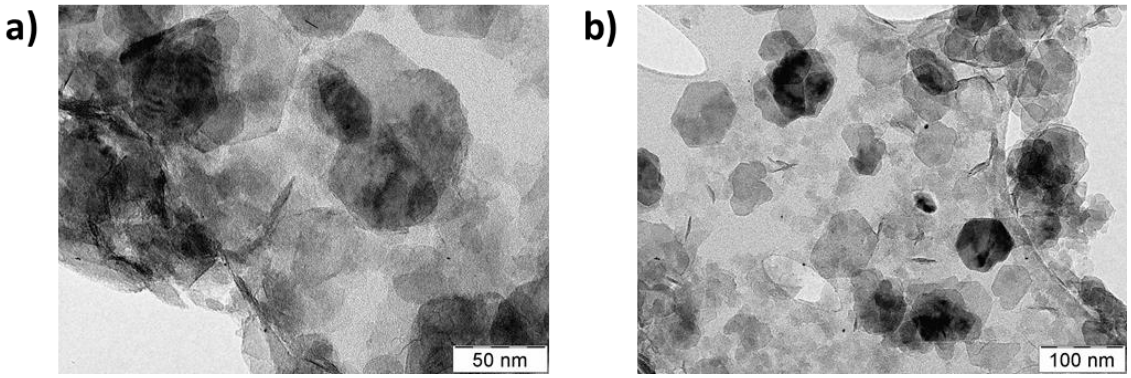

Figure 33. Transmission Electron Micrographs (a,b) of the synthesized anodic catalyst NiFe (LDH).

The TEM images of anodic catalyst NiFe at different magnifications were reported in Figure 33a-b. The morphology of the NiFe oxide-hydroxide (LDH) catalyst showed a mixture of small circular shape particles. The majority of these particles had a dimension of less than 4-5 nm.

Once the synthesis protocol was optimized, the next step was to expand the NiFe oxide-hydroxide (LDH)-based anode catalyst to maintain the good physicochemical characteristics, catalytic activity and stability achieved in small batches for the oxygen evolution reaction in an alkaline environment. Scale-up of the synthesis (from 2g to 6g) was carried out with the same experimental procedure but with larger amounts of reagents. NiFe-LDH was synthesized in small (2 g) and medium batches (6 g).

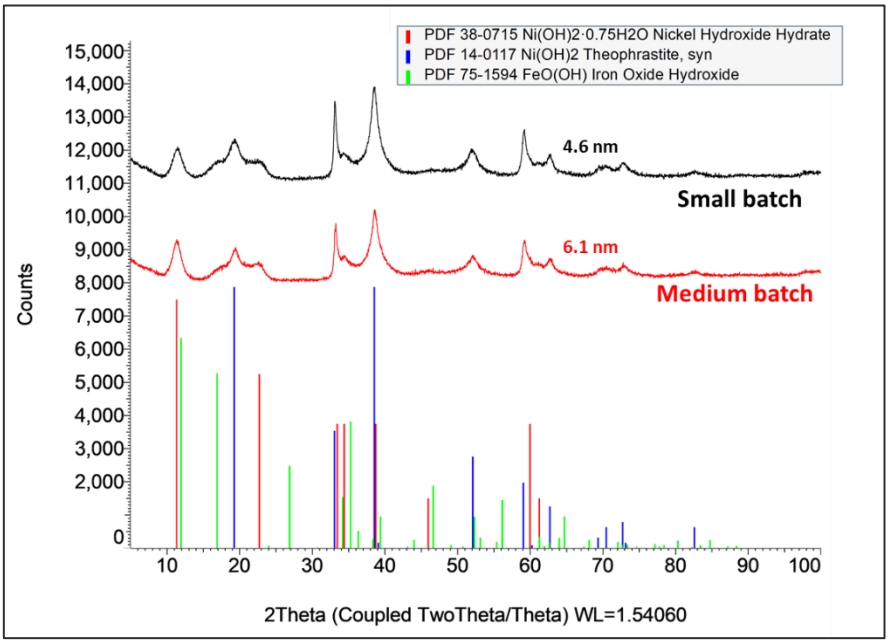

Figure 34. XRD patterns of the anodic batches synthesized NiFe oxide-hydroxide.

Various characterization techniques, including X-ray diffraction (XRD) and X-ray fluorescence (XRF) have been employed to investigate the physicochemical properties of the synthesized electrocatalysts. The XRD technique was utilized to obtain the crystalline phases of the developed catalysts. The XRD patterns reported in Figure 34 show the diffractograms of the comparison between small and medium batches synthesized. It is possible to notice that the medium batch (6g) and small batch (2g) have same physicochemical properties.

From XRF investigations it was analysed the catalyst elemental composition, and it was obtained the semi-quantitative results on the atomic ratio of Ni:Fe oxide-hydroxide. The compositions of the small and medium batches synthesized catalysts were showed in Table 11.

Table 11. Elemental composition (% wt.) of anodic electrocatalysts determined by XRF analysis.

NiFe LDH	Quantity (g)	Ni (% wt.)	Fe (% wt.)
Small batch	2 g	85.24	14.74
Medium batch	6 g	85.18	14.82

3.1.2 Nickel-Manganese Layered Double Hydroxide (NiMn-LDH)

Synthesis protocol (CIDETEC)

The NiMn-LDH catalyst was synthesized by a hydrothermal method. Specifically, a nickel and molybdenum precursors, along with urea, were dissolved in ultrapure water and loaded into a Teflon-coated stainless-steel autoclave. The autoclave was placed in an oven, kept under static conditions at the desired temperature for a specified period. Afterwards, the autoclave was removed from the oven and cooled to room temperature. The contents of the autoclave were then filtered under vacuum, recovering a brown-green solid. The solid was washed using an ultrasonic bath, first three times with UWP and then twice with ethanol. Finally, the material was dried in an oven overnight.

Physicochemical characterization of obtained catalyst

The crystalline structure of the catalyst is confirmed by X-ray diffraction (XRD), as shown in Figure 35. The diffractogram reveals a mixture of NiMn-LDH and $MnCO_3$ phases (PDF#01-084-6999). For the LDH phase, peaks at 11.4°, 22.8°, 34.3°, 38.3°, 38.7°, 45.9°, 59.5°, and 60.7° correspond to the (003), (006), (009), (012), (018), (110), and (113) planes, respectively. In contrast, the $MnCO_3$ phase displays peaks at 24.34°, 31.5°, 37.5°, 41.6°, 45.3°, 49.9°, 51.9°, and 67.9°, which correspond to the (012), (104), (110), (113), (202), (024), (116), and (300) planes, respectively. The crystallite size of the NiMn-LDH phase, estimated using the Scherrer equation, is approximately 13.6 nm, with lattice parameters a = b = 3.1 Å and c = 23.3 Å, indicating that CO_3^{2-} is the interlayer anion. For $MnCO_3$, the crystallite size ranges from 18 to 28 nm, with lattice parameters a = b = 4.8 Å and c = 15.6 Å. For both phases, the experimental parameters are consistent with theoretical values. Overall, the XRD analysis indicates that the current synthesis protocol produces a mixture of NiMn-LDH and $MnCO_3$, highlighting the need for tuning reaction temperature, precursor ratios, or reaction time to favor the LDH formation.

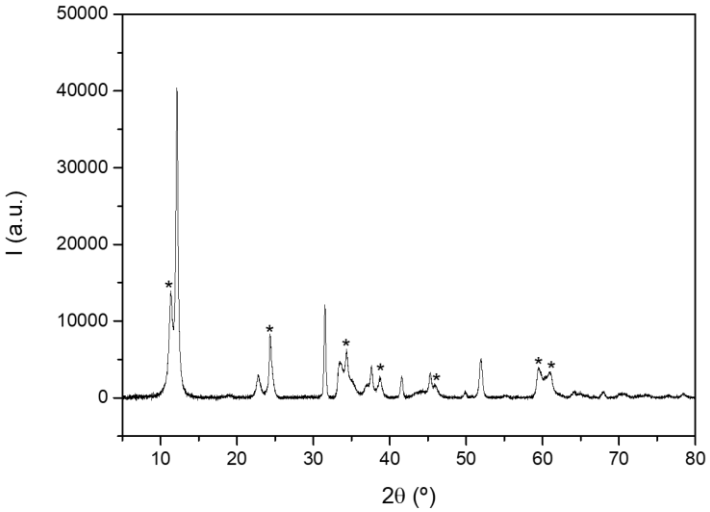

Figure 35. X-ray diffraction patterns of NiMn-LDH. The asterisks indicate reflections corresponding to the LDH phase.

3.1.3 NiFe spinels

Synthesis protocol (CIDETEC)

The NiFe spinel was synthesized from the NiFe-LDH materials prepared using protocol B.1 (as described in section 3.1.1.) and subsequently calcined in air at different temperatures.

Physicochemical characterization of obtained catalyst

Figure 36a shows the diffraction pattern characteristic of cubic NiFe spinel. The main diffraction peaks appear at 2θ values of 18.8°, 30.2°, 35.7°, 37.2°, 43.2°, 57.4°, 62.9°, 75.3°, and 79.3°, corresponding to the (111), (220), (311), (222), (400), (511), (440), (622), and (444) planes, respectively (PDF#00-010-0325). The crystallite size is estimated to be 8.8 nm using the Scherrer equation, with lattice parameters a = b = c = 8.3 Å, in agreement with theoretical values for the cubic spinel structure.

Figure 36b shows a SEM image, revealing that the material is composed of small primary nanoparticles which aggregate into larger structures. The surface appears rough and porous, with irregularly shaped agglomerates distributed across the sample. The elemental composition determined by EDX and XRF is summarized in Table 12. Although oxygen is not detectable by XRF, a direct comparison with the EDX results (excluding oxygen, i.e., 73.6 % wt. Ni and 26.4 % wt. Fe) shows good agreement between both techniques. Based on the EDX weight percentages, the estimated stoichiometry corresponds approximately to $NiFe_{0.4}O_{1.4}$ composition.

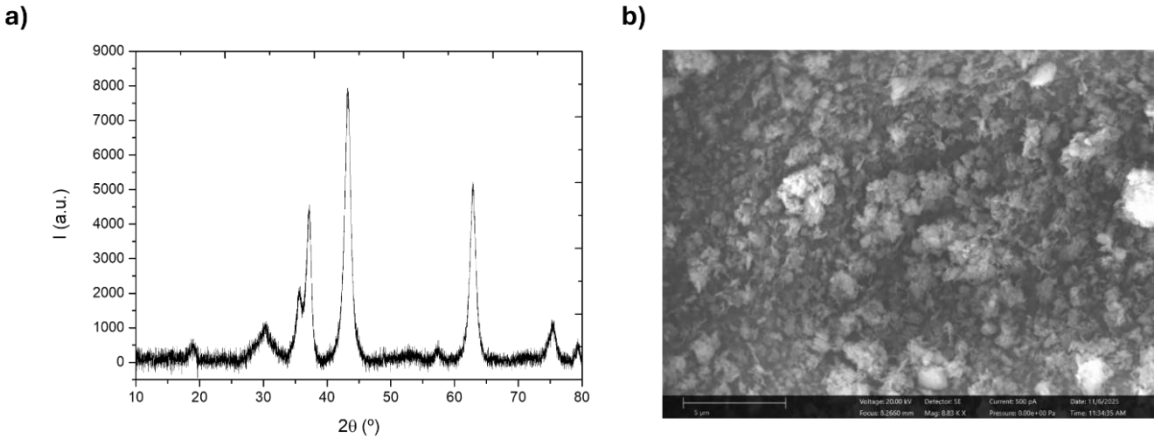

Figure 36. X-ray diffraction pattern (a) and SEM image (b) of NiFe spinel.

Table 12. Elemental composition (% wt.) of the NiFe spinel determined by EDX and XRF analyses.

EDX (% wt.)			XRF (% wt.)		
Ni	**Fe**	**O**	**Ni**	**Fe**	**O**
58.8	21.1	22.1	71.9	28.2	n.d.*

*n.d.: not detected, indicating that the element is below the detection limit of the technique.

3.1.4 Co_3O_4 – Benchmark anode catalyst

The commercial Co_3O_4 (Cobalt(II, III) oxide, Puratronic™, 99.9985%, Alfa Aesar) was used as a commercial benchmark anode catalyst.

Physicochemical characterization of benchmark anode catalyst (CNR)

The benchmark catalyst was characterized physiochemically through X-ray diffraction (XRD) and Scanning electron microscopy (SEM/EDX).

XRD technique was utilized to evaluate the crystalline phase of the catalysts developed and the Figure 37 shows the diffraction pattern of commercial catalyst. The main diffraction peaks appear at 2θ values of 19°, 31.3°, 36.8°, 38.5°, 44.8°, 55.6°, 59.3°and 65.2° Bragg angles (PDF 42–1467). The peaks are highly broadened with a crystallite size of 35 nm.

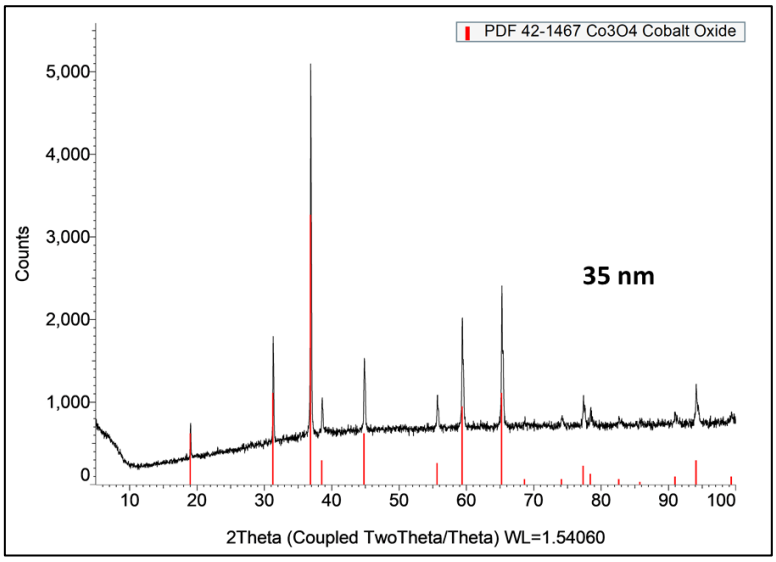

Figure 37. XRD pattern of the commercial anode *catalyst* Co_3O_4.

The benchmark anode catalyst was characterized through scanning electron microscopy (SEM) and energy-dispersive X-ray (EDX) analysis. The EDX probe was used to determine the bulk elemental composition of the samples.

Scanning electron micrographs of the commercial catalyst were reported in Figure 38a-c. The weight percentage of Co and O was observed by SEM-EDX analysis (Table 13).

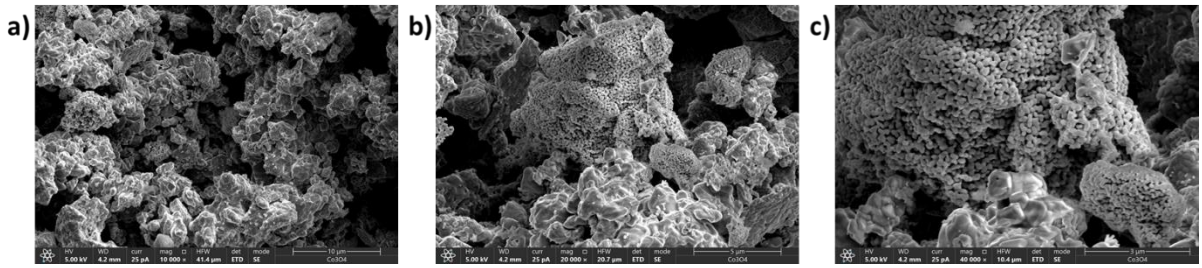

Figure 38. Scanning Electron Micrographs (a-c) of the commercial anode *catalyst* Co_3O_4.

Table 13. Elemental composition (% wt.) of the commercial anode catalyst Co_3O_4 determined by EDX analysis.

Sample	EDX (% wt.)	
	Co	O
Co_3O_4	90.27	9.73

3.2 PGM-free self-standing cathode electrocatalysts

3.2.1 Nickel nanoPTL@Ni_3S_2

Synthesis of nickel nanoPTL (SINTEF)

Ni nanoPTL was first prepared in a custom-made reactor with steady temperature control and rotating magnetic field (Figure 39). Nickel salt, stabilising agent, nucleating agent, and reducing agent was all mixed and reacted at 80 °C for one hour or until all the reactants were consumed. The prepared nanoPTL was washed, dried, and cut to size for further modifications or performance valuation.

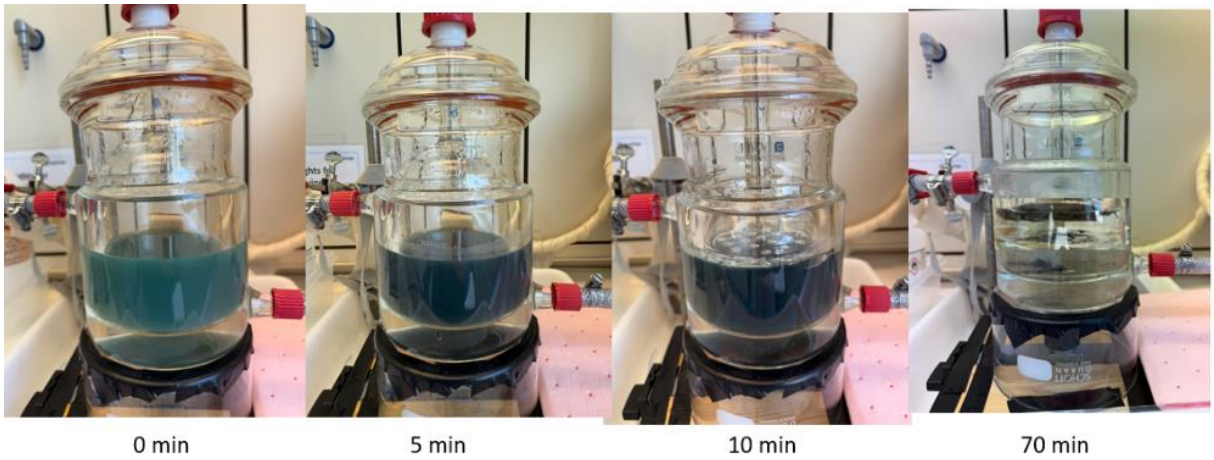

Figure 39. Photographs of chronological progress within the reactor during synthesis.

Synthesis of nanoPTL@Ni_3S_2 (SINTEF)

The Ni nanoPTL was first sintered to enhance electrical connectivity of the nanofibers prior to sulfidation. Ni nanoPTL was placed in a tube furnace and sintered at 350 °C in reducing atmosphere (5% H_2 in Ar). The sintered nanoPTL was then placed in an autoclave with sulphur containing solution and reacted for 2 hours at moderate temperature to minimize embrittlement from excessive sulphur penetration. The resulting nanoPTL@Ni3S2 was rinsed and dried prior to testing.

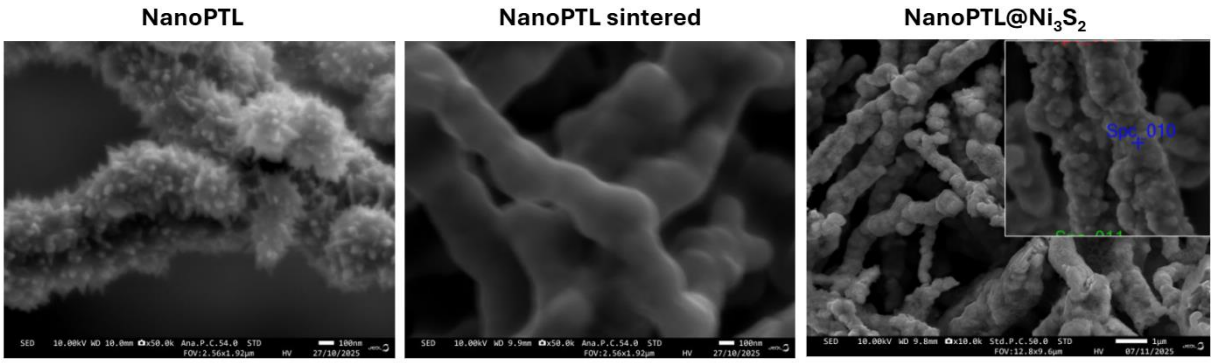

Figure 41. SEM images of NanoPTL, sintered NanoPTL, and NanoPTL@Ni_3S_2.

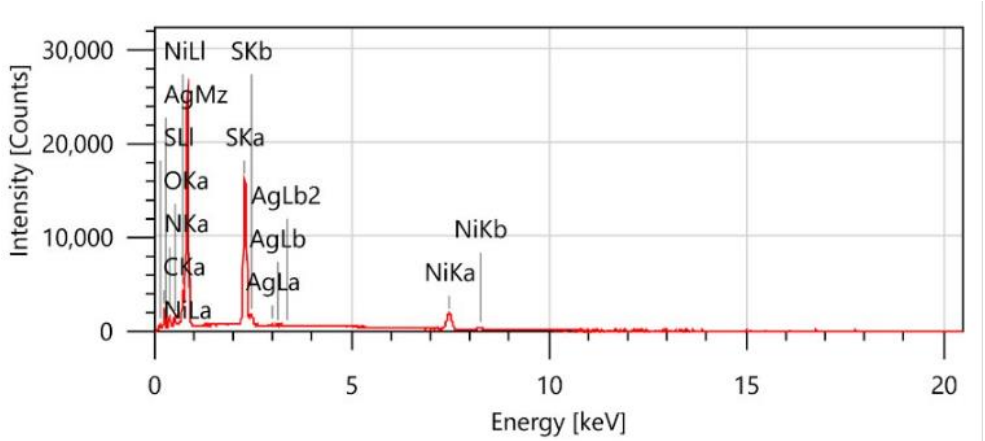

Element	Line	Mass%	Atom%
C	K	3.09±0.02	11.54±0.07
N	K	2.52±0.03	8.05±0.08
O	K	0.56±0.01	1.57±0.03
S	K	11.50±0.04	16.07±0.06
Ni	K	82.23±0.84	62.74±0.64
Ag	L	0.10±0.02	0.04±0.01
Total		100.00	100.00
Spc_012			Fitting ratio 0.0181

Figure 40. EDS spectra and mass and atomic composition of nanoPTL@Ni_3S_2.

SEM images (Figure 41) show that sintering smooths out the rough surface structure of the nanoPTL, and sulfidation partially restores some surface area losses. EDS indicates clear presence of sulphur post sulfidation. XRD (Figure 42) confirms that with the optimal sulfidation conditions, Ni_3S_2 shell on the nanoPTL skeleton structure is achieved. Further optimisation with secondary atom doping, such as Fe or Mo by incorporation during sulfidation will be explored to enhance the catalytic activity.

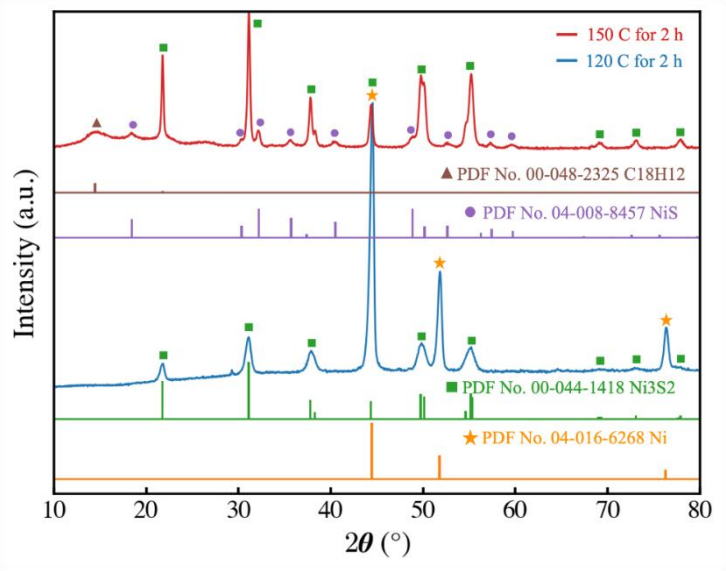

Figure 42. XRD spectra of Ni nanoPTL@Ni_3S_2 in different sulfidation conditions.

3.2.2 Electrodeposited Ni-based alloys (Ni-X-Y, X=Mo, W, Co; Y=S)

Electrodeposition process and characterization (CIDETEC)

Ni-based alloys with transition metals as well as phosphides, chalcogenides are promising choices for OER catalysis integrated into self-standing or porous electrode architectures. Among various options, Ni-Mo and Ni-Mo-S alloys initially developed for HER, can be also suitable for catalysing OER reaction, as it has been demonstrated in literature. Therefore, the synthesis and physic-chemical characterization of the catalysts reported in *Section 2.2* is still relevant for OER catalysts.

Nickel-tungsten (Ni-W) and nickel-cobalt (Ni-Co) electrocatalysts are highly promising for the oxygen evolution reaction (OER) in alkaline water electrolysis due to their enhanced catalytic activity and durability. Both electrocatalysts can be engineered as self-standing electrodes or coatings with porous architectures, suitable for scalable alkaline electrolyzers. Here, Ni-W and Ni-Co films were electrodeposited in a two-electrode cell using carbon cloth fibres as substrate.

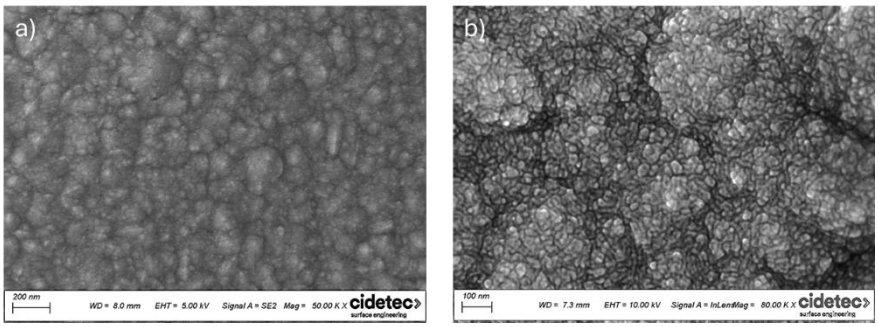

Figure 43. Representative surface morphology images of free-standing OER electrocatalysts: (a) Ni-W with fully dense structure and (b) Ni-Co alloy with mesoporous structure.

Figure 43 shows the representative surface morphology images of the obtained Ni-W and Ni-Co electrocatalysts. The surface of Ni-W exhibits a compact, granular and nodular morphology. It is composed of spherical or globular grains without cracks or pores. The surface of Ni-Co shows a reticulated or web-like structure due to the presence of mesopores induced by the P123. The pores appearance is similar to a "spider web" with clear boundaries between the globular domains.

SEM cross-sectional characterization of these samples shown in Figure 44 and reveals that the catalyst is successfully metalized the fiber substrate. During the substrate pre-conditioning a thin layer of electroless Ni was deposited to improve the conductivity and adhesion of the electrodeposited Ni-W alloy catalyst. The Ni-W electrodeposition resulted in a clear bilayer structure, where the Ni-W coating was observed on top of the Ni-P metallization layer. EDX point analysis further confirmed the successful incorporation of W into the electrodeposited layer, reaching 15 wt.%. The W content can be further increased up to 30 wt.% by adjusting electrodeposition conditions. Likewise, the Co content in Ni-Co alloy was varied between 10-50 wt.%.

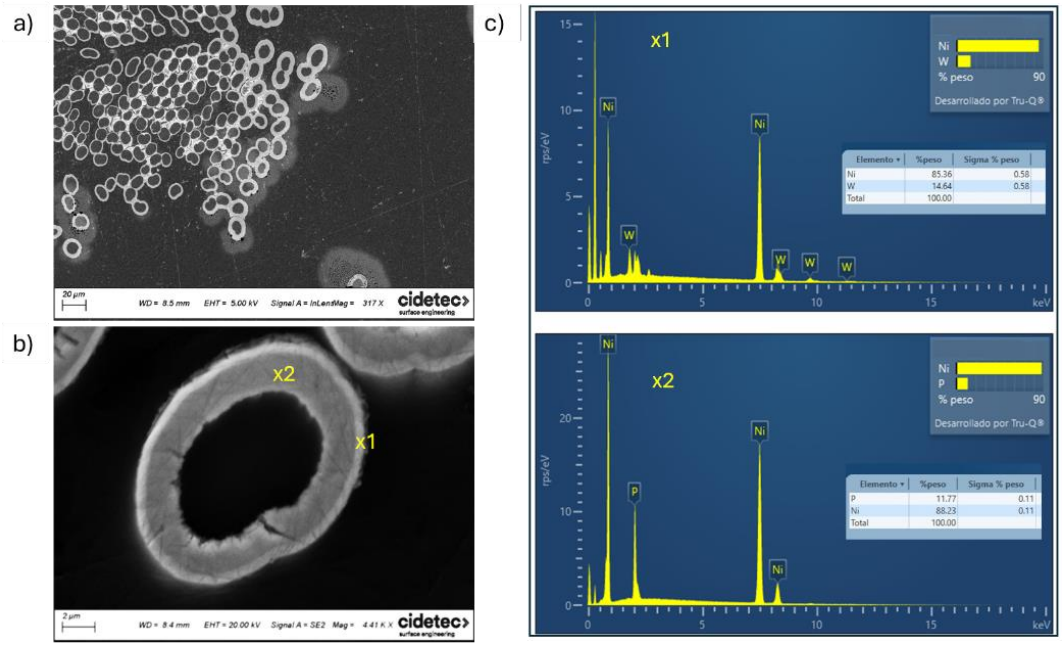

Figure 44. Cross section of Ni-W free standing electrode composed of C cloth substrate, Ni-P adhesive layer and Ni-W catalyst layer: (a) low magnification image showing the cross-section of a bunch of fibers, (b) cross-section of an individual fiber; and (c) EDX point analysis realized on the section of individual fiber, as marked in Panel (b).

3.2.3 Electroless Ni-P alloy

Electroless process and characterization (CIDETEC)

Nickel phosphorous alloy electrocatalysts are widely studied for their excellent performance in OER. The unique electronic structure arising from the interaction between nickel and phosphorus atoms enhances catalytic activity by optimizing hydrogen adsorption and desorption processes. Ni-P electrocatalysts typically exhibit high catalytic activity, low overpotential, and good stability across a

range of pH conditions. To provide an alternative for the catalysts screening in SWEETHY, the Ni-P electrocatalysts were prepared by electroless deposition. By this method a thin layer of metal grows onto the surface of a substrate without the need for an external electrical power source as a result of an autocatalytic reaction. Compared to electrodeposition methods, electroless processes can be used to coat the non-conductive surfaces and achieve a better uniformity on the substrates with complex 3D structures, and it is fully deployed at industrial scale.

The content of incorporated P plays a significant role in the resulting properties of the alloy. Therefore, two compositions of Ni-P where targeted: (i) low P content, i.e. 2-4 wt.% (Ni-LP), (ii) high P content, i.e. 12-14 wt.% (Ni-HP). CIDETEC has many years of experience working with electroless Ni-P deposits, mainly seeking for corrosion resistant coatings. Several plating baths using hypophosphite ions as reducing agent have been previously developed at CIDETEC and demonstrated their applicability to prepare the Ni-P layers with tailored multifunctional properties at industrial scale. Therefore, for each targeted alloy composition a specific bath has been formulated. This allowed to always work under optimized conditions regardless of the targeted concentration of P in the deposit. Polyurethane foams (PUF) have been considered as an appropriate substrate that could provide the desired level of macroporosity to the electrodes. Electroless plating onto a non-conductive surface, like PUFs, requires a series of steps to deposit a thin metallic layer onto the non-conductive material, thus involving a series of substrate pre-treatments steps (such as degreasing and activation). Figure 45a shows the representative porous structure of PUF metallized with electroless Ni-P. Figure 45b and c show the typical morphology of Ni-P alloy with low and high P content, respectively.

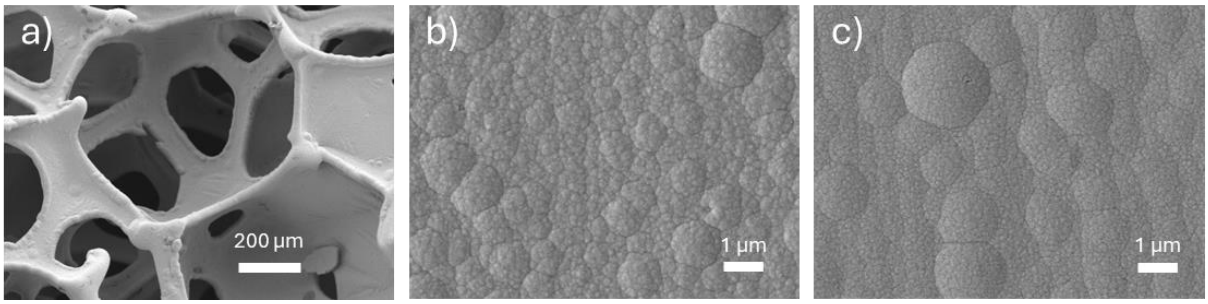

Figure 45. Representative SEM images of electroless Ni-P alloys: (a) low magnification image showing the macroporous structure of the obtained Ni-P foam; (b) surface morphology detail of low-P Ni-P alloy; (c) surface morphology of high-P Ni-P alloy.

4 Contribution to project Specific Objectives

The reported results make a substantial contribution to the overall objectives of the SWEETHY project, particularly to Specific Objective 1 (SO1), while also providing foundational input for subsequent objectives (SO2–SO4).

Contribution to SO1: *Develop high-performance, cost-effective and durable materials for direct seawater AEMWE components.*

The activities reported in this deliverable directly address the identification, development and optimization of suitable PGM-free electrocatalysts for the hydrogen and oxygen evolution reactions (HER and OER) under seawater-relevant conditions, as well as definition and characterization of the benchmark catalyst materials. By focusing on non-noble transition-metal-based systems and employing scalable wet-chemistry and electrodeposition methods, the materials are designed to resist chloride-induced corrosion and degradation typical of saline operation. The structural, morphological, and compositional characterisation presented here ensures that only the most promising formulations will proceed to in-situ electrochemical screening.

The catalyst composition prioritizes non-critical, earth-abundant elements and low-cost, scalable synthesis routes. These approaches align with SWEETHY's goal of reducing the Levelized Cost of Hydrogen (LCOH) through both material substitution (avoiding PGM and CRM) and process efficiency (using mild synthesis conditions and aqueous precursors).

Contributions to other objectives (SO2–SO4). Although focused on catalyst preparation and ex-situ assessment, Deliverable 3.1 also lays the foundation for later project objectives:

- It provides quality materials for integration and testing in the AEMWE short stack (SO2).
- It supports cost and sustainability assessments by providing PGM-free catalyst formulations and scalable synthesis routes (SO3, SO4).
- It contributes to the environmental targets of SWEETHY by promoting CRM-free compositions and low-impact synthesis, ensuring alignment with the project's sustainability principles.

5 Contribution to major project exploitable result

Deliverable 3.1 contributes to several of SWEETHY's exploitable results by generating and validating knowledge, materials, and methodologies that contribute to the development of the project's seawater electrolysis prototype. Specifically, the outcomes of this deliverable support the following key exploitable results:

Development of PGM-free HER and OER catalysts for direct seawater operation: The synthesis and structural optimisation of transition-metal-based catalysts constitute a core exploitable result. The deliverable provides a set of formulations suitable for further electrochemical validation and scale-up. These materials represent a viable alternative to PGM-based catalysts, offering significant potential for cost reduction and reduced dependence on critical raw materials.

Scalable and sustainable catalyst synthesis routes: The deliverable demonstrates wet-chemistry and electrodeposition-based fabrication methods that are compatible with industrial upscaling. These routes minimise the use of hazardous reagents, contributing to SWEETHY's goal of environmentally sustainable manufacturing. This knowledge will be exploitable in both future catalyst production and industrial AEMWE manufacturing lines.

Foundation for next-stage component integration and testing: Some of the identified and characterised catalysts from Deliverable 3.1 will feed directly into WP6 for integration into large-area electrodes and MEAs, forming the active layers of the SWEETHY short stack. Thus, this deliverable provides a critical input for achieving high-efficiency and durable AEMWE prototypes under real seawater operation — one of the project's major exploitable outputs.

Scientific and technological know-how: The developed materials design strategies (e.g., nanostructure control, alloying, surface treatments) represent valuable intellectual and scientific assets that can be exploited through publications, patents, and future collaborations. These insights advance the state of the art in electrocatalysis for harsh environments and position the SWEETHY consortium as a strong player in direct seawater electrolysis materials.

6 Conclusion and Recommendation

Various powder-based and self-standing catalysts were successfully synthesized and characterized for further validation as HER or OER electrocatalysts in seawater electrolyser environments. The catalyst development focused on using non-critical, earth-abundant elements and scalable, low-cost fabrication methods, primarily wet-chemistry synthesis and electrodeposition. The prepared catalysts exhibited controlled composition, morphology and microstructure enabling optimization for electrocatalytic performance.

Benchmarks were established with Pt/C as the cathode catalyst and Co_3O_4 as the anode catalyst. For the cathode, key catalysts included Ni- and Mo-sulfides, electrodeposited alloys, and Mo carbide, aligning with transition metal compounds known to exhibit promising hydrogen evolution reaction activity. On the anode side, Ni-based spinels, NiFe layered double hydroxides, Ni sulfides, and alloys with W, Co, Mo, and P were developed to withstand the strongly oxidizing and saline conditions typical of seawater electrolysis, with particular attention on catalyst stability and corrosion resistance.

Overall, the deliverable demonstrates a comprehensive electrocatalyst preparation framework combining advanced synthesis methods aimed at high-performance, stable and scalable catalysts for seawater electrolysis applications. This supports the project's strategic goal of developing PGM-free, cost-effective, and durable catalysts that meet industrial requirements for sustainable hydrogen production in challenging environments.

7 Risks and interconnections

During M01-M10, no foreseen risks related to WP3 activities have been materialized. No unforeseen risks to report.

7.1 Interconnections with other deliverables

The catalysts developed and characterized in this deliverable will be screened in seawater conditions. The results will be reported in ***D3.2 Catalyst screening in seawater*** in M12.

8 Acknowledgement

The author(s) would like to thank the partners in the project for their valuable comments on previous drafts and for performing the review.

Project partners:

#	Partner short name	Partner Full Name
1	RISE	RISE RESEARCH INSTITUTES OF SWEDEN AB
2	CNR	CONSIGLIO NAZIONALE DELLE RICERCHE
3	CIDETEC	FUNDACION CIDETEC
4	DLR	DEUTSCHES ZENTRUM FUR LUFT- UND RAUMFAHRT EV
5	IC	INSTITUT DE LA CORROSION SASU
6	SINTEF	SINTEF AS
7	PROPULS	PROPULS GMBH
8	CENMAT	CUTTING-EDGE NANOMATERIALS CENMAT UG HAFTUNGSBESCHRANKT
9	UNR	UNIRESEARCH BV

Disclaimer/ Acknowledgment

The project is supported by the Clean Hydrogen Partnership and its members.
Co-funded by the European Union under Grant Agreement No. 101192342. The views and opinions expressed are those of the author(s) only and do not necessarily reflect those of the European Union or the Clean Hydrogen Partnership. Neither the European Union nor the granting authority can be held responsible for them.